

Elsevier Editorial System(tm) for Geochimica
et Cosmochimica Acta

Manuscript Draft

Manuscript Number: GCA-D-18-00380R2

Title: Cu and Zn isotope fractionation during extreme chemical weathering

Article Type: Article

Corresponding Author: Dr. Susan Halsall Little, Ph.D

Corresponding Author's Institution: University College London

First Author: Susan Halsall Little, Ph.D

Order of Authors: Susan Halsall Little, Ph.D; Sophie Munson; Julie Prytulak; Barry J Coles; Samantha J Hammond; Mike Widdowson

Abstract: Copper and Zn are trace metal micronutrients whose stable isotope systematics are receiving increasing attention as possible paleoenvironmental tracers. However, to realise this potential, their behaviour during chemical weathering must be better constrained. We present coupled Cu and Zn isotope data for a well-characterised Indian laterite weathering profile, which includes a full suite of samples from unaltered greywacke bedrock to indurated lateritic duricrust. This sample set provides an exceptional opportunity to interrogate Cu and Zn isotope compositions during an extreme example of chemical weathering. Despite their occurrence in different host phases within the parent greywacke, Cu and Zn isotopes behave coherently during weathering. We observe preferential loss of heavy isotopes at increasing degrees of alteration, with 0.6% total variability in $\delta^{66}\text{Zn}$ and 0.9% in $\delta^{65}\text{Cu}$. Given the absence of evidence for CuS or ZnS phases in the parent lithology, we attribute the liberation of heavy isotopes to organic complexation in the aqueous phase and/or incorporation of light isotopes in secondary aluminous Fe-oxides. Strong enrichment of both metals is also associated with a peak in Mn at a previously identified paleo-water table horizon. This dataset confirms that weathering under oxygenated conditions releases isotopically heavy Cu, regardless of the host phase. Meanwhile, Zn isotopes are only fractionated to any significant extent at the most extreme degrees of chemical weathering reached during lateritization. We conclude that the isotopic composition of the weathering-derived input of Zn to rivers should be largely insensitive to climate change on geological timescales.

Cu and Zn isotope fractionation during extreme chemical weathering

Susan H. Little^{1,2*}, Sophie Munson², Julie Prytulak³, Barry J. Coles², Samantha J. Hammond⁴, Mike Widdowson⁵

1. Department of Earth Sciences, University College London, Gower Place, London, WC1E 6BS, UK.

*susan.little@ucl.ac.uk

2. Department of Earth Science and Engineering, Royal School of Mines, Imperial College London, London, SW7 2BP, UK.

3. Department of Earth Sciences, Durham University, Durham DH1 3LE, UK.

4. Department of Environment, Earth and Ecosystems, The Open University, Walton Hall, Milton Keynes, MK7 6AA, UK.

5. School of Environmental Sciences, Cohen Building, University of Hull, Hull, HU6 7RX, UK.

23 July 2019

For resubmission to *Geochimica et Cosmochimica Acta*

Abstract

Copper and Zn are trace metal micronutrients whose stable isotope systematics are receiving increasing attention as possible paleoenvironmental tracers. However, to realise this potential, their behaviour during chemical weathering must be better constrained. We present coupled Cu and Zn isotope data for a well-characterised Indian laterite weathering profile, which includes a full suite of samples from unaltered greywacke bedrock to indurated lateritic duricrust. This sample set provides an exceptional opportunity to interrogate Cu and Zn isotope compositions during an extreme example of chemical weathering. Despite their occurrence in different host phases within the parent greywacke, Cu and Zn isotopes behave coherently during weathering. We observe preferential loss of heavy isotopes at increasing degrees of alteration, with 0.6‰ total variability in $\delta^{66}\text{Zn}$ and 0.9‰ in $\delta^{65}\text{Cu}$. Given the absence of evidence for CuS or ZnS phases in the parent lithology, we attribute the liberation of heavy isotopes to organic complexation in the aqueous phase and/or incorporation of light isotopes in secondary aluminous Fe-oxides. Strong enrichment of both metals is also associated with a peak in Mn at a previously identified paleo-water table horizon. This dataset confirms that weathering under oxygenated conditions releases isotopically heavy Cu, regardless of the host phase. Meanwhile, Zn isotopes are only fractionated to any significant extent at the most extreme degrees of chemical weathering reached during lateritization. We conclude that the isotopic composition of the weathering-derived input of Zn to rivers should be largely insensitive to climate change on geological timescales.

Keywords: Cu, Zn, Isotopes, Laterite, Weathering, Organic complexation, Fe oxides

1 **1.0 Introduction**

2
3 Variations in the stable isotope ratios of the bioessential transition metals Zn and Cu
4 are increasingly being utilised as tracers of past Earth surface processes, particularly
5 in the ocean (e.g., Kunzmann et al., 2013; Pons et al., 2013; Chi Fru et al., 2016; John
6 et al., 2017; Isson et al., 2018). However, while isotopic shifts in sedimentary records
7 of both Zn and Cu are undoubtedly present during periods of global change (e.g.,
8 Snowball Earth events in the Neoproterozoic), and often tantalisingly systematic (e.g.,
9 Kunzmann et al., 2013; John et al., 2017), their underlying controls remain difficult to
10 elucidate.

11
12 Paleooceanographic interpretations of observed Zn and Cu isotope variations can be
13 divided into one or more of three main causal categories. (1) Invoking a change in
14 biological productivity (or other related process) in the ocean itself (Kunzmann et al.,
15 2013; Isson et al., 2018). (2) Suggesting a change in the balance of the removal fluxes
16 to different oceanic sinks, for example, due to a change in ocean redox state (Chi Fru
17 et al., 2016; John et al., 2017). (3) Interpretations that require a change in the
18 magnitude or isotopic composition of a *source* of the element to the ocean, for
19 example, a change in the weathering-derived flux due to tectonic or climate change
20 (Kunzmann et al., 2013; Pons et al., 2013; Chi Fru et al., 2016).

21
22 Weathering of the continents supplies solutes to rivers, which constitute a key input of
23 Zn and Cu to the modern ocean (Little et al., 2014b). The Zn and Cu isotope
24 composition of rivers will thus reflect that supplied by weathering, though
25 biogeochemical processes in rivers may subsequently modify this primary signature
26 (e.g., Borrok et al., 2008; Coutaud et al., 2014; Szyrkiewicz and Borrok, 2016;
27 Coutaud et al., 2018). The aim of this study is to investigate Zn and Cu isotope
28 fractionation during extreme chemical weathering. This approach provides an end-
29 member constraint on the degree of isotope fractionation possible in the weathering
30 environment. It is a starting point from which to evaluate the leverage of chemical
31 weathering in modifying the isotopic composition of rivers through time, and hence
32 its possible influence on the wider marine inventory.

33

34 A study of the dissolved phase in rivers found a discharge-weighted Zn isotope
35 composition unfractionated from continental rocks (Little et al., 2014b). The absence
36 of systematic Zn isotope fractionation in rivers implies little or no Zn isotope
37 fractionation during weathering, a hypothesis partially supported by studies of Zn
38 isotopes in soils (Bigalke et al., 2010a; Vance et al., 2016; Opfergelt et al., 2017; Suhr
39 et al., 2018). However, studies carried out in extreme, (sub-) tropical weathering
40 regimes have observed preferential release of heavy Zn isotopes (Viers et al., 2007;
41 Lv et al., 2016; Guinoiseau et al., 2017; Suhr et al., 2018). This observation has been
42 explained by various processes, including release of isotopically heavy Zn during
43 oxidative weathering of sulphides (Fernandez and Borrok, 2009; Lv et al., 2016);
44 organic complexation of the heavy isotope in the dissolved pool (Guinoiseau et al.,
45 2017); incorporation or adsorption of isotopically light Zn in/on clays (Viers et al.,
46 2007; Guinoiseau et al., 2017) or Fe oxides (Viers et al., 2007; Suhr et al., 2018); or
47 release of isotopically light Zn from refractory mineral phases and subsequent re-
48 precipitation with Fe oxide phases (Suhr et al., 2018).

49

50 In contrast to Zn, Cu in the riverine dissolved pool is isotopically heavy relative to
51 rocks (Vance et al., 2008); this behaviour is similar to observations for Mo (Archer
52 and Vance, 2008; Neubert et al., 2011), Li (Huh et al., 1998), Ni (Cameron and
53 Vance, 2014), and Cr isotopes (Frei et al., 2014). Accordingly, there are two proposed
54 explanations for the heavy Cu isotope composition in rivers: (1) An equilibrium
55 isotope fractionation in rivers (Vance et al., 2008) and/or in soils (Vance et al., 2016)
56 between an isotopically heavy, organic ligand bound, dissolved pool and an
57 isotopically light pool sorbed to particulates; (2) Redox-driven release of isotopically
58 heavy Cu during oxidative weathering of sulphides in black shales or supergene
59 systems (Mathur et al., 2005; Mathur et al., 2012; Mathur and Fantle, 2015; Lv et al.,
60 2016).

61

62 The present study investigates the Zn and Cu isotope systematics of a well-
63 characterised Indian lateritic weathering profile. The term laterite is not always used
64 ubiquitously or consistently. We follow the definition in the widely cited
65 *Encyclopaedia of Geomorphology* (Goudie, 2004; Widdowson, 2004), which states
66 that: 'Laterite is an iron-rich, sub-aerial, weathering product, commonly believed to

67 evolve as a result of intense, *in situ* substrate alteration under tropical or sub-tropical
68 climatic conditions.’ A lateritic weathering profile therefore constitutes a chemical
69 residuum resulting from the relative enrichment of relatively immobile elements
70 (notably Fe and Al), as described initially by Newbold (1844), and more recently by
71 many other authorities (e.g., McFarlane, 1976; McFarlane, 1983; Schellman, 1983;
72 Aleva, 1984; Widdowson, 2004, 2007; Babechuk et al., 2014). This definition
73 emphasises the relative enrichment of Fe (and Al) through desilication processes
74 involved in the development of a laterite profile; this enrichment/depletion may be
75 modified through hydromorphism associated with oscillating redox conditions in the
76 developing weathering profile and typically driven by pluvial seasonality and
77 associated water-table recharge.

78

79 Laterites typically form on parent lithologies with inherently high iron contents (such
80 as mafic and ultramafic igneous rocks and chemically immature sediments) and on
81 stable continental landmasses subject to high mean annual temperatures, high
82 humidity and seasonal, high annual rainfall (Widdowson, 2007). These climatic
83 conditions promote intense *in situ* chemical weathering and mineral alteration,
84 making laterites an ideal natural laboratory to study the weathering process *in*
85 *extremis*. Today, laterites and associated weathering products account for
86 approximately 30% of Earth surface cover, and almost 50% of continental drainage
87 flows over these terrains (Tardy, 1997).

88

89 To date, two studies have reported Zn isotope data from lateritic weathering profiles,
90 one developed on granodiorite in Cameroon (Viers et al., 2007) and the other for the
91 Bidar laterite developed on Deccan basalt in central India (Suhr et al., 2018). Both
92 studies observe preferential retention of light Zn isotopes in the laterite residues. To
93 the best of our knowledge, no Cu isotope data for laterites has yet been reported.

94

95 **2.0 Geological setting and background**

96

97 **2.1 Geological setting**

98

99 The coastal lowlands of western peninsular India between $\sim 8^\circ$ and $\sim 19^\circ\text{N}$ comprise
100 dissected, laterite-capped ‘tablelands’ with maximum altitudes of $\sim 150\text{--}200\text{m}$ in the
101 east systematically descending to less than $50\text{--}100\text{m}$ at the coastline (Widdowson,
102 2009). These tablelands are remnants of a once extensive laterite belt that extended
103 along the length of western peninsular India (Widdowson, 2009), developed upon a
104 variety of lithologies. This belt provides evidence of an important phase of Cenozoic
105 lateritization that affected western India during the latest Eocene to the Miocene
106 (Schmidt et al., 1983; Bonnet et al., 2014), when climatic conditions were optimal for
107 deep weathering (Tardy et al., 1991).

108

109 The site of the investigated profile lies in the small coastal state of Goa. Metamorphic
110 rocks of varying grade and composition dominate the geology of Goa (Pascoe, 1950)
111 and include weakly metamorphosed Dharwar sediments of the Dharwar craton,
112 including abundant Late Archaean greywackes (Argast and Donnelly, 1986; Devaraju
113 et al., 2010; Dessai, 2011). The samples in this study (hereafter referred to as ‘SQ’)
114 are from a quarried laterite profile developed upon meta-greywackes of the
115 Sanvordem Fm (of the Proterozoic age Dharwar Supergroup; $> 2.5\text{ Ga}$) at Merces
116 village, near Panjim Goa ($15^\circ 28' 44''\text{N}$, $73^\circ 52' 35''\text{E}$; Fig. 1).

117

118 The parent greywacke consists of a detrital assemblage of quartz, feldspar and
119 volcanic rock fragments (Srinivasan et al., 1989) and geochemical analysis suggests
120 that the bulk sediment was derived from submarine weathering of a felsic volcanic
121 source (Devaraju et al., 2010). Sparse biotite has developed in response to low-grade
122 thermal metamorphism of unknown age. The SQ laterite profile itself is of probable
123 Oligocene-Miocene age (c. $35\text{--}20\text{ Ma}$; Schmidt et al., 1983; Bonnet et al., 2014),
124 and developed upon the low-lying coastal (Konkan) plain, subsequent to erosion (i.e.
125 removal of c. $1\text{--}1.5\text{ km}$ thickness) across the Indian continental margin (Widdowson,
126 1997; Widdowson and Gunnell, 1999).

127

128 **2.2 Sample description**

129

130 The lithology and mineralogy of the 34 m thick laterite profile has previously been
131 reported in Wimpenny et al. (2007) as the SQ samples series, and comprehensively in
132 Hibbert (2017) as an independent MQ sample series. A schematic diagram of the SQ

133 profile is shown in Figure 2 (mineralogy and major element data from Wimpenny et
134 al., 2007). Samples SQ2 – SQ14 were sampled from increasingly shallow depths and
135 represent a greywacke parent that has undergone increasing degrees of alteration
136 (Table S1; Figs. 2, 3). Sample SQ1 was taken from a small mafic dyke, which cuts
137 unaltered greywacke near the base of the profile. All samples have previously been
138 analyzed for major element (Table S2) and high-precision trace element
139 concentrations (Table S3) (Howarth et al., 2018; Wimpenny et al., 2007).

140

141 Deep lateritic weathering profiles such as the one described here have considerable
142 antiquity and affect the substratum far below that of modern pedogenetic processes.
143 The degree of alteration progresses upward from unaltered ‘parent’ material, through
144 saprock to saprolite, through a ‘mottled zone’, and ultimately to the topmost Fe-rich
145 laterite duricrust (i.e. ‘carapace’ and then indurated ‘cuirasse’ in the francophone
146 terminology).

147

148 Saprock (from the Greek ‘*sapros*’ meaning ‘rotten’) is the first stage of weathering: It
149 consists of partially weathered minerals and as yet unweathered minerals (e.g.,
150 feldspars have begun to alter to clay minerals and/or olivine to iddingsite). Saprock
151 maintains all the fabrics and features of the fresh rock, and is distinguished from the
152 more advanced stage of saprolite by retaining much of its original physical strength,
153 and some primary mineralogy. Saprolite is more altered than saprock but, like
154 saprock, there has been little or no change in bulk volume, and the distribution of
155 resistant minerals remain more or less in position as they occurred in the parent.
156 Weatherable minerals in saprolite are typically wholly pseudomorphed by clays
157 and/or oxides and oxyhydroxides, whilst the original rock fabric remains largely
158 preserved (Taylor and Eggleton, 2001). In the zone of alternating reduction and
159 oxidation due to repeated wetting and drying, segregation of iron occurs, forming
160 ‘mottles’. The uppermost laterite duricrust hardens irreversibly due to complete
161 drying and oxic conditions, and consists predominantly of crystallised Fe and Al
162 oxide and oxyhydroxides.

163

164 The SQ profile can be divided into four zones of alteration (Figs. 2, 3), as defined by
165 Wimpenny et al. (2007):

166 Zone I, at 34 – 15m depth (samples SQ2 – SQ6), exhibits no alteration (parent rock)
167 or low degrees of alteration while retaining the primary texture and fabric of the
168 bedrock (saprock);
169 Zone II, at 15 – 8.5m depth (samples SQ7 – SQ9), consists of altered saprolite in
170 which most weatherable primary minerals are destroyed, then passing into a ‘mottled’
171 region, in which secondary minerals and Fe-Al-rich accretions (i.e. mottles) form;
172 Zone III, at 8.5 – 7m depth (samples SQ10 and SQ11), is a narrow zone thought to be
173 influenced by a paleo-water table (Wimpenny et al., 2007);
174 Zone IV, at 7m – surface (samples SQ12 – SQ14), is the Fe-rich cap in which
175 secondary minerals are removed and the Fe-Al-rich accretions fuse to form a resistant,
176 indurated laterite duricrust.
177 The ‘line of seepage’, at ~15m depth, divides little altered greywacke (zone I) from
178 the zones of increasing alteration above, and is so-called because it marks a
179 significant increase in porosity and permeability (Wimpenny et al., 2007).
180
181 The mineralogical changes that occur upwards in the profile (Table S1, Fig. 3) are
182 reflected in variations in major element concentrations (Table S2, Fig. 2),
183 characterized by a general decrease in Si and concomitant enrichment in Fe and Al
184 (Wimpenny et al., 2007; Widdowson, 2009). In the low alteration zone I, the range of
185 major element concentration variations are somewhat limited (Table S2, Fig. 2) and
186 are likely related to lithological heterogeneity in the parent greywacke (Widdowson,
187 2009). Above the line of seepage, in zones II and IV, there is an increasing degree of
188 depletion of more mobile elements (e.g., Si, Mg, Ca, Na, K), due to the formation and
189 then breakdown and removal of secondary clay minerals, generating the observed
190 enrichment of less mobile elements (e.g., Fe, Al and Ti) in the residue (Widdowson,
191 2009). Notably, this broad pattern is interrupted at ~7 – 8.5m depth (zone III; samples
192 SQ10 and 11) by significantly elevated concentrations of Fe and Mn and depletion of
193 Al; previously interpreted as the depth of a paleo-water table (Fig. 2; Wimpenny et
194 al., 2007).
195
196 Trace element concentrations exhibit similar coherent trends as the rock becomes
197 increasingly altered in zones II-IV (Wimpenny et al., 2007; Howarth et al., 2018).
198 Some fluid-mobile elements (e.g., Li, Rb, Ba, Cu, Zn) show a general decrease in
199 concentration towards the surface but a pronounced peak at the paleo-water table (Fig.

200 S1A). Other fluid mobile elements, particularly the REE and PGEs, show enrichment
201 at the paleo-water table and in zone IV (Fig. S1B), this is attributed to mobilization in
202 low pH, high Eh conditions below, followed by scavenging from solution and
203 incorporation in the oxide phases that precipitate above (Wimpenny et al., 2007). By
204 contrast, relatively immobile elements (e.g., Zr, Ti, Nb) display a general increase in
205 concentration towards the surface and a pronounced concentration decrease at the
206 paleo-water table (Fig. S1C).

207

208

209 **3.0 Analytical Methods**

210

211 **3.1 Sulphur analyses**

212

213 Sulphur concentrations were measured on an aliquot of solution previously digested
214 for high precision trace element analysis (see Howarth et al., 2018, for details on
215 digestion techniques). Analyses were conducted on an Agilent triple quadrupole ICP-
216 MS (ICP-QQQ) at the Open University. For conventional ICP-MS systems measuring
217 sulphur concentrations has been challenging, owing to the high background
218 contribution (from O₂). The ICP-QQQ has an octopole reaction system (ORS) that
219 separates two quadrupole mass filters, allowing for targeted interference removal. For
220 S we use O₂ as the reactive gas, forming SO⁺ as the product in the ORS, and measure
221 the mass shifted oxide ion (i.e. at mass 50 for ³⁴S). This effectively reduces the
222 background from ~1.1 x 10⁴ cps to ~2 x 10² cps. Detection limits are 0.2 ng/g in the
223 solutions (equivalent to 0.2 µg/g in the rock – samples are diluted 1000 fold prior to
224 analysis). Analyses were standardised against a suite of five reference materials
225 (BIR-1, W-2, BHVO-2, AGV-1, BE-N) measured at the start of each analytical
226 session. An internal standard solution was also bled in online throughout the
227 analytical session, and used to monitor and correct for instrument drift. In addition, a
228 monitor block, consisting of BHVO-2 (digested at Imperial College with the
229 unknowns and not used in the calibration) BE-N and 2% HNO₃ was run every 4 – 5
230 unknowns to further monitor drift, and to monitor precision and accuracy of
231 measurements.

232

233 The reference materials used in the calibration have only information values listed in
234 the GEOREM database (and where uncertainties are quoted these are also large, e.g
235 BHVO-2 = 164 ± 25 $\mu\text{g/g}$). However, for the majority of materials we find that using
236 these information values yields a calibration line with an R^2 value of 0.9995. We also
237 find that rock reference materials behave very similarly to the samples during
238 ionisation in the plasma, and therefore find this a more robust method of calibrating
239 rather than having to apply an ionisation correction to a suite of synthetic calibration
240 materials. The one outlier from our calibration line is BIR-1. Further investigation by
241 standard addition methods indicate that the concentration of S is 4.5 $\mu\text{g/g}$ in three
242 further BIR-1 digests from our powder aliquot (rather than 70 $\mu\text{g/g}$ as quoted from
243 GEOREM) and, when this is taken into account, the BIR-1 measurements again sit on
244 the calibration line as described above, and do not alter the R^2 value of the line. We
245 find that our repeat measurements of the BHVO-2 standard digested at Imperial
246 College show both a precision and accuracy of <4 % (RSD) compared to the
247 information values given. Whilst some caution must be exercised in using these
248 information values, we remain confident in the relative concentration variations
249 within our sample suite.

250

251 **3.2 Zn and Cu isotope analyses**

252

253 All isotopic analytical work was carried out in the MAGIC clean laboratories at
254 Imperial College London using deionized 18.2 M Ω water (MQ), Teflon-distilled acids
255 (HF, HNO₃ and HCl), Suprapur H₂O₂, and acid-cleaned Savillex PFA labware. 20 mg
256 of each sample was digested in a $\sim 3:1$ HF:HNO₃ mix at 140°C for ~ 48 hours. After
257 drying down to a gel-like consistency, samples were treated three times with
258 concentrated HNO₃ to drive off fluoride salts. Previously published high precision
259 trace element data for the same sample powders (Howarth et al., 2018) were used to
260 estimate the appropriate volume of a ^{64}Zn - ^{67}Zn double spike required to obtain a Zn
261 spike:sample ratio of approximately 1.2 (Arnold et al., 2010; Bridgestock et al.,
262 2014). After spike equilibration, conversion to chloride, and re-dissolution in 7M HCl
263 + trace H₂O₂, Cu and Zn fractions were purified from the same digest solutions via
264 anion exchange using AG MP-1M resin (BioRad), as detailed previously (Maréchal et
265 al., 1999; Archer and Vance, 2004; Little et al., 2014b). Due to the highly refractory
266 nature of the samples (i.e. high concentrations of potentially interfering elements such

267 as Ti and Fe), three column passes were performed for both the Cu and Zn fractions.
268 The final Zn column was smaller in volume, following Bridgestock et al. (2014).

269

270 Prior to analysis, purified Cu fractions were refluxed overnight in HNO₃ + H₂O₂ and
271 purified Zn fractions were treated twice with ~100 μL HNO₃, with the intention of
272 eliminating residual resin-derived organics, before final re-dissolution in 1 mL 2%
273 HNO₃. Aliquots of these solutions were diluted to final concentrations of ~100ppb
274 total Zn (i.e. spike + sample Zn) and ~100ppb Cu for analysis. For both Cu and Zn,
275 the USGS rock standards BHVO-2, BIR-1A, BCR-2 and Nod-P1 were processed
276 using the same procedures and analysed to assess accuracy. Table 3 compares our
277 data with previously published δ⁶⁶Zn and δ⁶⁵Cu values.

278

279 Zinc isotope analyses followed protocols described previously (Arnold et al., 2010;
280 Bridgestock et al., 2014). Briefly, measurements were made on a Nu Plasma HR MC-
281 ICP-MS equipped with an ARIDUS II (CETAC Technologies) desolvating system
282 and nominal 100 μL/min MicroMist glass nebulizer, in low resolution mode.

283 Instrumental sensitivities were >100 V/ppm Zn. Data collection (3 × 20 5s
284 integrations) was preceded by an analysis (15 5s integrations) of the 2% HNO₃ used
285 to dilute solutions, with subtraction of these “on-peak zeroes” from sample signals.

286 Instrumental mass bias was corrected via the double spike technique described in
287 Arnold et al. (2010) and Bridgestock et al., (2014). Data reduction was carried out
288 offline following Siebert et al. (2001), with corrections for spectral interferences from
289 ⁶⁴Ni (via monitoring ⁶²Ni) and Ba²⁺ ions (via monitoring at mass 68.5). Interference
290 corrections were negligible, however, with ⁶⁴Ni⁺/⁶⁴Zn⁺ and ¹³⁴Ba²⁺/⁶⁷Zn⁺ levels at less
291 than 1 × 10⁻⁵ in all cases. The Zn isotope ratios of samples were determined relative
292 to matching (spike:natural Zn ratio and total Zn) standard solutions of IRMM-3702:

293 Eqn. 1: $\delta^{66}\text{Zn} = [(R_{\text{Sample}}/R_{\text{Standard}}) - 1] \times 1,000$

294 Final values are reported normalised to JMC Lyon by applying a correction of
295 +0.30‰, as recommended in the recent review by Moynier et al. (2017). Over the
296 course of this study the long-term reproducibility of a secondary standard, the in-
297 house ‘London Zn’, was $\delta^{66}\text{Zn}_{\text{JMC-Lyon}} = +0.08 \pm 0.07\text{‰}$ (n = 99, 2 SD), compared
298 with $+0.08 \pm 0.04\text{‰}$ (n = 10, 2 SD) reported by Arnold et al. (2010) and $+0.12 \pm$
299 0.04‰ (n = 6, 2 SD) by Larner and Rehkämper (2012). Total procedural blanks for

300 Zn were 3.6 ± 2.6 ng ($n = 8$, 1 SD), less than 1% of the Zn content of the smallest
301 sample. Yields were $104 \pm 10\%$ (1 SD).

302

303 Copper isotope analyses employed a Nu Plasma II HR MC-ICP-MS at Imperial
304 College London. Measurements were made in low resolution mode, with introduction
305 via a Peltier cooled (to 5°C) glass spray chamber coupled to a ~ 100 $\mu\text{L}/\text{min}$ glass
306 nebulizer. Instrumental mass bias was corrected via doping with Ni following e.g.,
307 Ehrlich et al. (2004) and Larner et al., (2011). Nickel was chosen ahead of Zn for this
308 study because it has a first ionization potential (7.64 eV) close to that of Cu (7.72 eV)
309 and it is less sensitive to contamination. All samples and standards were doped to
310 achieve a Ni:Cu ratio of 3 to 4, matched to within $\pm 5\%$. Tests at variable Ni/Cu ratios
311 (2 to 5) suggested that neither accuracy nor precision is sensitive to the selected Ni:Cu
312 ratio. Analyses were carried out in static mode using Faraday cups to monitor masses
313 60, 61, 62 (for Ni), and 63, 65 (for Cu).

314

315 Data collection consisted of 60 x 5s integrations preceded by an analysis (15 x 5s
316 integrations) of the 2% HNO_3 solution, with the latter subtracted from sample signals.
317 Sensitivity for Cu was typically ~ 25 V/ppm. The exponential law was used to mass
318 bias correct measured $^{65}\text{Cu}/^{63}\text{Cu}$ ratios relative to $^{62}\text{Ni}/^{60}\text{Ni}$. $\delta^{65}\text{Cu}$ values were then
319 calculated as the deviation of the mass bias corrected $^{65}\text{Cu}/^{63}\text{Cu}$ ratio of the sample
320 relative to two bracketing standards (ERM-AE633):

321 Eqn. 2: $\delta^{65}\text{Cu} = [(R_{\text{Sample}}/R_{\text{ERM-AE633}}) - 1] \times 1,000$

322 This combination of external element doping and standard-sample bracketing has
323 previously been described for e.g., Tl with Pb (Nielsen et al., 2004) and for Cu with
324 Ni (Larner et al., 2011).

325

326 Finally, the minor reported offset of -0.01‰ between AE633 and the international
327 standard NIST SRM 976 was applied, such that data are reported normalised to SRM
328 976 (Moeller et al., 2012). The long-term reproducibility of a secondary Romil Cu
329 solution standard was $\delta^{65}\text{Cu}_{\text{SRM-976}} = +0.23 \pm 0.07\text{‰}$ ($n = 22$, 2 SD), comparable to
330 the $+0.20 \pm 0.08\text{‰}$ ($n = 5$, 2 SD) reported by Larner et al. (2011). Total procedural
331 blanks for Cu were 4.9 ± 1.7 ng ($n = 4$, 1 SD), less than 1% of the Cu content of the
332 smallest sample. Yields, estimated by comparison of Cu concentration data from the

333 OU (Howarth et al., 2018) with concentrations from the isotopic analysis (obtained by
334 a less precise beam matching approach), were $93 \pm 9\%$ (1 SD). Complete yields are
335 essential for Cu isotope analyses due to the potential for isotopic fractionation during
336 anion exchange (Maréchal and Albarède, 2002); no relationship is observed between
337 sample isotopic composition and calculated yield, corroborating the accuracy of the
338 Cu isotope data presented here.

339

340 **3.3 Calculating CIA, IOL and τ –values**

341

342 Two useful measures of the degree of weathering are presented. First, the Chemical
343 Index of Alteration (CIA) is calculated following Nesbitt and Young (1982). CIA
344 utilises the molar mass of key indicator elements:

345 Eqn. 3: $CIA = [Al_2O_3 / (Al_2O_3 + CaO^* + Na_2O + K_2O)] \times 100$

346 [Where each compound is expressed as its molar mass]

347 CaO* is the amount of CaO incorporated in the silicate fraction of the rock. Since
348 CaO contents of the SQ samples are low (<1 wt%), and because inherent carbonate
349 phases were absent, no correction for the sample carbonate content was deemed
350 necessary. CIA effectively tracks feldspar dissolution and the concomitant release of
351 Ca, Na, and K relative to Al, since the latter is typically retained within resulting
352 clays. Most igneous rocks of varying composition will plot between a CIA value of 35
353 and 55, with mafic rocks occupying the lower values. Unaltered granites and
354 granodiorites, which may be representative of the greywacke protolith of the SQ
355 profile, have CIA values of between 45 and 55. By comparison, sample SQ2 has a
356 CIA value of 57 (Table 2; Fig. 2).

357

358 Second, Babechuk et al., (2014) suggest an alternative means to chemically
359 characterise the stages of extreme weathering at which the CIA becomes ineffective,
360 the Index of Lateritisation (IOL; Table 2, Fig. 2):

361 Eqn. 4: $IOL = 100 \times [(Al_2O_3 + Fe_2O_{3(T)}) / (SiO_2 + Al_2O_3 + Fe_2O_{3(T)})]$

362

363 Enrichment or depletion of an element can be quantified by comparison to an
364 immobile reference element. For this purpose, we calculate the tau (τ) parameter
365 (after Chadwick et al., 1990):

366 Eqn. 5: $\tau_{i/j} = \left[\frac{(C_i)_h}{(C_i)_p} \right] - 1$

367 Where C is the measured concentration, i is the element of interest (e.g., Zn, Cu), j is
368 an immobile reference element (Nb, Ti or Zr), h is the weathering product, and p the
369 unaltered parent lithology. A value greater than zero indicates net gain of an element
370 relative to the parent material at that horizon within the weathering profile, while a
371 value less than zero indicates loss.

372

373 Two approaches were used to investigate uncertainty in τ –values. First, we compared
374 τ -values calculated assuming p is represented by the deepest sample in the section
375 (SQ2) with those calculated by taking an average of all samples from the little altered
376 zone I (SQ2 – SQ6). Second, Babechuk et al. (2014) advocate the use of Nb as the
377 most appropriate immobile reference element (j) for lateritic sample suites. In
378 addition, and for comparison, we compare τ -values calculated using Nb with those
379 determined using immobile elements Ti and Zr. Importantly, we find no significant
380 difference in absolute values or patterns of elemental enrichment or loss independent
381 of the choice of p or j (Fig. S2, Fig. 4).

382

383

384 **4.0 Results**

385

386 **4.1 Zn and Cu concentrations and enrichment-depletion patterns (τ -values)**

387

388 Copper concentrations exhibit limited absolute variability up-section (31 – 66 $\mu\text{g/g}$)
389 compared to larger variations in Zn (21 – 146 $\mu\text{g/g}$) (Table 2, Fig. 4A). Both Cu and
390 Zn concentrations decrease in stepwise fashion across the line of seepage, which
391 represents the transition from zone I to zone II at ~15m depth (Fig. 4A). Elevated
392 concentrations of both elements are observed at 7.5m (zone III, sample SQ11), the
393 uppermost depth of the paleo-water table (Wimpenny et al., 2007). The surface-most
394 sample (SQ14) has distinctly higher Cu and Zn concentrations compared to the other
395 two samples beneath; together these three samples make up the Fe-rich duricrust
396 (zone IV).

397 Both τ_{Zn} and τ_{Cu} become increasingly negative up section, with up to ~90% Zn and
398 ~70% Cu depletion relative to the protolith composition (Fig. 4B). The pattern of
399 enrichment and depletion of both elements above the line of seepage (at ~15m) is
400 similar, with marked depletion immediately above this transition, interrupted by a
401 sharp peak of enrichment at the paleo-water table, followed by more moderate
402 enrichment in the uppermost sampling horizon (SQ14, particularly evident for τ_{Cu}).
403 τ_{Zn} exhibits a very strong correlation with τ_{Li} throughout the laterite profile, while τ_{Cu}
404 is decoupled from both τ_{Li} and τ_{Zn} in zone I, at 15m and below (Fig. 4B).

405

406 **4.2 Zn and Cu isotope systematics**

407

408 The unaltered greywacke protolith, represented by sample SQ2 at 34 m, has a Zn
409 isotope composition of $+0.50 \pm 0.04\text{‰}$ ($n = 2$, 2SD). This value is isotopically heavy
410 compared to typical lithogenic Zn in clastic sediments, at $+0.28 \pm 0.13\text{‰}$ ($n = 105$,
411 Moynier et al., 2017). For Cu, sample SQ2 has a Cu isotope value of $+0.03 \pm 0.05\text{‰}$
412 ($n = 2$, 2SD), which is within the typical range for Cu in clastic sediments at $+0.08 \pm$
413 0.20‰ ($n = 42$, Moynier et al., 2017).

414

415 In the low alteration zone I, below the line of seepage (samples SQ2 to SQ6, 34 to 15
416 m), Zn isotope ratios do not vary outside of analytical uncertainty ($\delta^{66}\text{Zn} = +0.47 \pm$
417 0.09‰ , $n = 5$, 2SD). Copper isotope ratios show a resolvable shift from ~0‰ at the
418 base of the profile to lower values at 22.5m (SQ5, -0.28‰) and 15m (SQ6, -0.23‰)
419 (Fig. 5A).

420

421 Above the line of seepage in zones II–IV (15 m – surface), samples SQ7 to SQ14
422 show considerably more marked, correlated shifts in Zn and Cu isotope compositions.
423 This is manifest as a general trend towards lower $\delta^{66}\text{Zn}$ and $\delta^{65}\text{Cu}$ upwards in the
424 weathering profile (Fig. 5). Again, the paleo-water table interrupts this trend in $\delta^{65}\text{Cu}$,
425 with a marked offset towards a higher Cu isotope ratio (at -0.30‰) compared to the
426 samples directly above and below (at -0.86‰ and -0.65‰ respectively). The surface-
427 most sample (SQ14) is isotopically lightest for both Cu (at -0.87‰) and Zn (at $-$
428 0.02‰). In summary, the total variability up section in $\delta^{65}\text{Cu}$ is 0.91‰ , which is
429 greater than that observed for $\delta^{66}\text{Zn}$, at 0.55‰ .

430

431

432 **5.0 Discussion**

433

434 **5.1 Zone I: Host phases and lithological heterogeneity in the low alteration zone**

435 **(parent – saprock)**

436

437 Wimpenny et al. (2007) described the mineralogical variations through the SQ
438 sequence, which we briefly recount here. The deepest greywacke sample (SQ2, 34 m)
439 comprises 75% quartz, 15% biotite, 5% plagioclase, 2% opaques and 3% other
440 minerals (Wimpenny et al., 2007). Up-section in zone I (SQ2 – SQ6 at 34 – 15m),
441 lithological variability is observed (Fig. 3). For example, biotite contents vary
442 between 8 and 20%, plagioclase from 2 – 8% and quartz from 74 – 80%. Secondary
443 clay minerals (e.g., kaolinite) are not observed in zone I (Fig. 3), confirming the
444 limited extent of chemical weathering at these depths. CIA values are consistent with
445 this inference, and remain essentially unchanged between the base of the profile (CIA
446 = 57 at 34m) to the top of zone I (CIA = 59 at 15m; Fig. 2)

447

448 Lithological variability is reflected in the major and trace element geochemistry of the
449 zone I samples. Al_2O_3 , Fe_2O_3 , MgO, Li and many other trace element concentrations
450 positively co-vary with biotite crystal content in this zone (Table S1, S3; Fig. S3).
451 SiO_2 concentrations show the opposite trend (Fig. S4). These observations are
452 consistent with known minor lateral variation in the quarry (Hibbert, 2017) and are
453 likely linked to a grain size control on mineralogy and geochemistry, as previously
454 recognised in sedimentary settings (e.g., Vdović et al., 1991; Roser et al., 1996;
455 Lupker et al., 2011). Accordingly, Al_2O_3 and SiO_2 contents generally correlate and
456 anti-correlate with grain size respectively, due to the predominance of aluminium-rich
457 phyllosilicates (like biotite) in the fine grain size fraction.

458

459 Zinc concentrations in zone I samples correlate with biotite content (Fig. S3B), as
460 well as with several trace elements and major oxides that are commonly hosted in
461 biotite, including Li, Co, Rb, Cs and Tl, MnO, MgO and K_2O (Fig. 6A, C, data from
462 Howarth et al., 2018). Potassium and Mg are both key structural components in

463 biotite ($K_2(Mg,Fe^{2+})_{6-4}(Fe^{3+},Al,Ti)_{0-2}[Si_{6-5}Al_{2-3}O_{20}](OH,F)_4$) (Deer et al., 1992).
464 Manganese and Li are commonly substituted into biotite octahedral sites, and Cs, Rb
465 and Tl commonly replace K in interlayer sites (Deer et al., 1992; Gomez-Gonzalez et
466 al., 2015). These observations suggest that the Zn present in the parent greywacke is
467 principally hosted within biotite.

468

469 Both Zn and Cu are chalcophile and, if sulphide phases were present, would be
470 expected to strongly partition into these phases. However, measured S concentrations
471 in the SQ profile are low (<0.1 wt%, Fig. 6, Table 2) and, while there is a positive
472 correlation between Zn and S concentrations in zone I samples (Fig. 6G), a negative
473 correlation is observed between Cu and S concentrations (Fig. 6H). This observation
474 appears to rule out the presence of CuS phases in the parent lithology. Furthermore,
475 Banks (1973) reports 116 – 316 $\mu\text{g/g}$ S in biotite, suggesting that biotite-hosted S
476 provides a satisfactory explanation for the correlation of Zn with S (Fig. 6G).

477

478 In contrast to Zn, Cu shows negative correlations with almost all elements in zone I
479 except SiO_2 and Na_2O (Fig. 6). As discussed, higher $\text{SiO}_2/\text{Al}_2\text{O}_3$ ratios likely reflect a
480 coarser grain size. Higher Na_2O contents in sandstone versus siltstone have been
481 hypothesised to reflect a greater abundance of detrital plagioclase (Roser et al., 1996),
482 but no correlation is observed between Na_2O and plagioclase abundance in the SQ
483 sample set. Plagioclase contains only scarce quantities of trace elements (Deer et al.,
484 1992), in any case, making this an unlikely Cu host. We conclude that identification
485 of the Cu host phase(s) requires detailed micro-analytical work that is beyond the
486 scope of this study. Nevertheless, we suggest that Cu is present in one or more detrital
487 phase(s), the abundance of which is greater in the coarser grained beds of the
488 greywacke.

489

490 To summarise, the τ_{Zn} and τ_{Cu} values in zone I samples similarly reflect primary
491 lithological heterogeneity of the greywacke, rather than recording any elemental mass
492 transfer. Thus, in order to take account of this heterogeneity in calculating τ -values,
493 we use an average of all samples in zone I as the best estimate of the parent material
494 ('p' in Eqn. 5). This approach, rather than simply selecting the least altered sample
495 SQ2, leads to a greater coherence of the calculated τ -profiles for different elements

496 (e.g., Zn cf. Li) and for the same element using different immobile reference elements
497 (e.g., Ti, Zr, 'j' in Eqn. 5; Fig. S2).

498

499 Isotopically, the greywacke $\delta^{65}\text{Cu}$ lies within the range of typical clastic sediments, at
500 about 0‰ (Moynier et al., 2017). For $\delta^{66}\text{Zn}$, however, it is isotopically heavy (e.g.,
501 sample SQ2 at +0.50‰) relative to lithogenic Zn (at about +0.3‰; Moynier et al.,
502 2017). Similarly isotopically heavy Zn has been observed in biotite-granites from the
503 Kaapvaal craton, South Africa (Doucet et al., 2018), from Taiwanese andesite,
504 sandstones and suspended river sediment (Bentahila et al., 2008), and in granitoids
505 from the Nyong Basin, Cameroon (Viers et al., 2007) and the Lachlan Fold Belt,
506 Australia and Black Hills, South Dakota, USA (Telus et al., 2012).

507

508 At 22.5m (sample SQ5), a small shift (of about -0.3‰) towards a lower $\delta^{65}\text{Cu}$ value
509 is observed (Fig. 5). This shift may either be a primary lithological signature, or
510 indicate the earliest detectable onset of oxic chemical weathering. Sample SQ5 has
511 the highest phyllosilicate abundance (sum of biotite, muscovite and chlorite, 23%;
512 Table S1, Fig. 3) and a slightly elevated CIA value (of 63; Table 2, Fig. 2) compared
513 to the other samples in zone I (at 12–15% and 57–59 respectively). The high
514 abundance of easily weatherable, fine fraction phyllosilicates increases the
515 susceptibility of this sample to alteration (Goldich, 1938).

516

517 Overall, elemental variations in the low alteration zone I can primarily be explained
518 by lithological heterogeneity in the parent greywacke. Copper and Zn isotopes in this
519 zone exhibit small shifts, either reflecting this lithological heterogeneity and/or early
520 stage chemical alteration. A greater spatial resolution of sampling in the quarry would
521 improve constraints on the importance of lateral variability and lithological
522 heterogeneity.

523

524

525 **5.2 Zones II and IV: the Mottled and Laterite Zones**

526

527 Above the line of seepage, the mottled and laterite zones (II and IV) are characterised
528 by depletion of Cu and Zn (observed in negative τ_{Cu} and τ_{Zn}) and isotopically light
529 $\delta^{65}\text{Cu}$ and $\delta^{66}\text{Zn}$ values (Figs. 4, 5). This pattern could reflect either (i) preferential

530 release of heavy isotopes during mobilization from (i.e. dissolution of) the host phase,
531 or (ii) isotope fractionation in the aqueous phase and/or during precipitation of
532 secondary Fe oxide phases.

533

534 *5.2.1 Isotope fractionation during host mineral dissolution*

535

536 Mineral dissolution may be accompanied by isotope fractionation. For example,
537 isotopically light Zn and Cu in weathered black shales from China and the USA have
538 been interpreted to result from preferential release of heavy Cu and Zn isotopes
539 during oxidative weathering of sulphide minerals (Mathur et al., 2005; Fernandez and
540 Borrok, 2009; Kimball et al., 2009; Mathur et al., 2012; Lv et al., 2016). However, the
541 greywacke lithology of the SQ laterite is sulphide-poor, and neither Cu nor Zn
542 appears to be dominantly hosted in a sulphide phase (Section 5.1).

543

544 The alternation of wet and dry seasons results in oscillating reducing and oxic
545 conditions in the developing weathering profile. Under water-saturated conditions, Fe
546 (as ferrous Fe^{2+}) is mobile, while during drier periods this Fe precipitates as ferric Fe
547 oxides, forming the Fe-rich mottles of zone II. Hence, redox changes play an
548 important role in mineral breakdown, the removal of mobile elements, and the
549 formation of secondary minerals enriched in Fe_2O_3 and Al_2O_3 . Zinc is not redox
550 active, but mobilization of Cu via Cu(II) reduction has been hypothesised for
551 waterlogged soils and wetland systems (Bigalke et al., 2010c; Bigalke et al., 2013;
552 Babcsányi et al., 2014). However, Cu(II) to Cu(I) reduction is associated with release
553 of the light isotope of Cu (Bigalke et al., 2010c; Bigalke et al., 2013; Babcsányi et al.,
554 2014). The preferential release of light Cu isotopes from host mineral phases via
555 Cu(II) reduction is inconsistent with the isotopically light solid residue observed in
556 the SQ laterite. Hence, though oscillating redox is an important process in
557 lateritization, alone it cannot explain the observed Zn and Cu isotope variations.

558

559 In abiotic, proton-promoted dissolution experiments investigating the release of Fe
560 from hornblende, a small light isotope fractionation is observed (Brantley et al.,
561 2001). Similar light isotope fractionation of Fe and Zn is observed during dissolution
562 of granite with HCl (Chapman et al., 2009; Weiss et al., 2014). This preferential
563 release of light isotopes during proton-promoted dissolution likely reflects a kinetic

564 isotope fractionation. Again, preferential mobilization of light isotopes is inconsistent
565 with the isotopically light residue observed in the SQ weathering profile.

566

567 In natural aqueous solutions both Zn and Cu are dominantly complexed to strong
568 organic ligands (McBride, 1981; Coale and Bruland, 1988; e.g., Bruland, 1989; Xue
569 et al., 1995; Moffett and Brand, 1996; Wells et al., 1998; Shank et al., 2004; Grybos
570 et al., 2007; Hoffmann et al., 2007; Vance et al., 2008). It is well documented that
571 mineral dissolution rates are enhanced above proton-promoted rates by the presence
572 of organic ligands, via a ligand-promoted dissolution mechanism (e.g., Berthelin and
573 Munier-Lamy, 1983; Amrhein and Suarez, 1988; Bennett, 1991; Welch and Ullman,
574 1993; 1996; 2000). For example, release of Cu from Columbia River Basalt was
575 elevated in a batch experiment containing an organic ligand (citrate) compared to the
576 inorganic control (Neaman et al., 2005b). At equilibrium, organic complexation is
577 associated with preferential chelation of heavy isotopes (Dideriksen et al., 2008;
578 Jouvin et al., 2009; Bigalke et al., 2010b; Morgan et al., 2010; Fujii and Albarede,
579 2012; Fujii et al., 2013; Sherman, 2013; Fujii et al., 2014; Ryan et al., 2014; Marković
580 et al., 2017). Therefore, at equilibrium, ligand-mediated dissolution should be
581 associated with release of isotopically heavy Zn and Cu, consistent with the observed
582 isotopically light laterite residue.

583

584 We model this scenario as a simple open-system Rayleigh distillation process in
585 Figure 7. In this model, we envisage that the isotopically heavy, organically
586 complexed pool is continuously removed from the profile under a constant
587 fractionation factor. For Zn, the Rayleigh model isotope fractionation factor that best
588 fits the data is of the order $\alpha = 1.0002$, i.e. $\Delta^{66}\text{Zn}_{\text{aqueous-solid}} \approx +0.2\text{‰}$ (Fig. 7A). For
589 Cu, the required fractionation factor is larger, at about $\alpha = 1.001$ or $\Delta^{65}\text{Cu}_{\text{aqueous-solid}} \approx$
590 $+1.0\text{‰}$ (Fig. 7B). The fractionation factors derived from the Rayleigh approach can
591 only be confidently ascribed meaning for a single-step process, e.g., mobilization
592 from the host mineral phase. Several processes are operating and, likely, fractionating
593 Zn and Cu isotopes during lateritization. Nevertheless, the Rayleigh model produces
594 an acceptable fit to the data in spite of its simplicity (Fig. 7), and we proceed to
595 compare our model-derived fractionation factors to those for organic complexation of
596 Zn and Cu in the literature.

597

598 The magnitude of Zn and Cu isotope fractionation on organic complexation is a
599 function of the stability constant of complex formation (Ryan et al., 2014; Marković
600 et al., 2017). Organic ligands in freshwater solutions fall into two categories: low
601 molecular weight organic acids (or 'L1-type' ligands, e.g., polyphenols, hydroxamate
602 siderophores), and soluble humic/fulvic acids (Harter and Naidu, 1995). While
603 humic/fulvic acids generally have relatively weak stability constants (at around $\sim 10^7 -$
604 10^9), L1-type ligands can be much stronger (up to $\sim 10^{25}$). Copper has a particular
605 affinity for strong organic ligands (as compared to, e.g., Zn and Cd; Benedetti et al.,
606 1995; Xue et al., 1995; McBride et al., 1997). Relatedly, the magnitude of isotope
607 fractionation for organic complexation is also larger for Cu compared to Zn
608 (Marković et al., 2017; cf. Ryan et al., 2014).

609

610 A fractionation factor $\Delta^{66}\text{Zn}_{\text{aqueous-solid}} \approx +0.2\text{‰}$ (Fig. 7A) is consistent with an
611 experimental estimate of isotope fractionation for Zn complexation with purified
612 humic acid ($\Delta^{66}\text{Zn}_{\text{humic-aquo}} = +0.24 \pm 0.06\text{‰}$; Jouvin et al., 2009). By comparison, the
613 larger fractionation factor for Cu ($\Delta^{65}\text{Cu}_{\text{aqueous-solid}} \approx +1.0\text{‰}$; Fig. 7B) implies
614 complexation by complexes stronger than humic acids, which have a reported range
615 in $\Delta^{65}\text{Cu}_{\text{humic-aquo}}$ of $+0.24$ to $+0.55\text{‰}$ (Bigalke et al., 2010b; Sherman, 2013; Ryan et
616 al., 2014). Sherman (2013) predicts a fractionation factor for a L1 ligand model
617 complex (Cu acetohydroxamate) of $\Delta^{65}\text{Cu}_{\text{hydroxamate-aquo}} = +1.1\text{‰}$, while Ryan et al.
618 (2014) measured fractionation factors of up to $+0.84\text{‰}$ for strong synthetic L1-type
619 ligands. Both of these estimates would be consistent with the Rayleigh model
620 prediction.

621

622 In practice, it is unclear if chemical equilibrium between the rock and aqueous phase
623 (or something approaching it) can be obtained during weathering. Contrary to the
624 predicted release of heavy isotopes during ligand-promoted dissolution, dissolution of
625 granite in the laboratory in the presence of oxalic acid resulted in release of
626 isotopically *light* Zn (Weiss et al., 2014). Similarly, Brantley et al. (2004) and
627 Wiederhold et al. (2006) observed release of isotopically light Fe in ligand-mediated
628 leaching experiments with hornblende and goethite, respectively. However, these
629 leaching experiments were not at equilibrium, and the observed light isotope
630 fractionation may reflect a kinetic control. By contrast, long duration experiments of

631 Wiederhold et al. (2006) did exhibit the predicted reverse trend, with isotopically
632 heavy Fe in solution. It remains to be determined whether these longer duration
633 experiments more closely reflect processes operating in more advanced (i.e., lateritic)
634 weathering environments.

635

636 Mineral dissolution rates in the lab are typically one to three orders of magnitude
637 faster than in the field (e.g., Swoboda-Colberg and Drever, 1993; Kump et al., 2000;
638 Brantley, 2003). In the lab, dissolution rates are thought to be interface-limited, i.e.
639 the rate of reaction is determined by the dissolution rate of the mineral (Brantley,
640 2003). By contrast, mineral dissolution rates in a transport-limited scenario are
641 controlled by the rate of diffusion or advection in solution (Brantley, 2003). Mineral
642 dissolution is likely predominantly interface-limited in the field (see discussion in
643 Kump et al., 2000), but it can be transport-limited at low water-rock flushing rates
644 (Schnoor, 1990; Kump et al., 2000). This difference may partially explain the offset in
645 lab and field-derived mineral dissolution rates, with transport-limited dissolution
646 operating more slowly than interface-limited dissolution (Kump et al., 2000).

647

648 Lateritic weathering is likely to occur in a transport-limited (also called “supply
649 limited”; West et al., 2005) weathering regime, with low denudation rates coupled to
650 high weathering intensity (White and Buss, 2014). Weathering fluxes in this scenario
651 reflect thermodynamic constraints, with chemical weathering reactions occurring
652 close to equilibrium (White and Buss, 2014). Indeed, this regime is sometimes
653 referred to as ‘local-equilibrium’ (Lebedeva et al., 2010; Brantley and Lebedeva,
654 2011). Hence, we suggest that transport-limited mineral dissolution may be associated
655 with equilibrium isotope fractionation, while interface-limited mineral dissolution will
656 typically be kinetically controlled (e.g., Brantley et al., 2004; Wiederhold et al., 2006;
657 Weiss et al., 2014). If this hypothesis were correct, ligand-mediated mineral
658 dissolution at equilibrium would promote release of heavy Zn and Cu isotopes,
659 consistent with observations in the SQ laterite (see also section 5.2.2). The corollary
660 of this hypothesis, however, would predict kinetic isotope fractionation (i.e.
661 mobilization of light isotopes) in kinetic-limited (or ‘weathering-limited’) regimes, in
662 which the physical removal of eroded material is faster than its breakdown by
663 chemical weathering. There is limited evidence for this prediction in Zn and Cu
664 isotope weathering studies to date. We return to this topic in section 5.4.1.

665

666 To summarise, the isotopically light compositions observed in the SQ laterite residue
667 may reflect ligand-mediated dissolution of their host phases, if dissolution is
668 occurring close to equilibrium in a transport-limited regime. By contrast, mobilization
669 via either a kinetic or reductive (in the case of Cu) mechanism would be associated
670 with preferential release of isotopically light Zn and Cu. In this case, the salient
671 isotope fractionation during lateritic weathering must occur after Zn and Cu
672 mobilization, in pore waters and/or during precipitation of secondary minerals.

673

674 *5.2.2 Isotope fractionation in the aqueous phase*

675

676 As discussed, Zn and Cu will be dominantly complexed by organic ligands in the
677 aqueous phase (e.g., McBride, 1981; Xue et al., 1995; Grybos et al., 2007; Hoffmann
678 et al., 2007), and organic complexation is associated with chelation of heavy Zn and
679 Cu isotopes (Jouvin et al., 2009; Bigalke et al., 2010b; Fujii and Albarede, 2012; Fujii
680 et al., 2013; Sherman, 2013; Fujii et al., 2014; Ryan et al., 2014; Marković et al.,
681 2017). By comparison, the free or weakly complexed pool of Zn or Cu will be
682 isotopically light. Taking Cu as an example, free Cu²⁺ and organically complexed Cu
683 and are isotopically offset by up to -1.1‰ (Sherman, 2013). In a closed system at
684 isotopic equilibrium, the Cu isotope composition of organically complexed Cu (δ_{org})
685 is constrained by this fractionation factor ($\Delta_{\text{free-org}}$) and the ratio of organically
686 complexed Cu to free Cu ($N_{\text{org}}/N_{\text{free}}$), as described by equation 6 (modified after
687 Stevenson et al., 2017):

688 Eqn 6:
$$\delta_{\text{org}} = \delta_{\text{system}} - \frac{\Delta_{\text{free-org}}}{1 + \frac{N_{\text{org}}}{N_{\text{free}}}}$$

689 In nature, $N_{\text{org}}/N_{\text{free}}$ for Cu is always very high – i.e. Cu is almost quantitatively
690 organically complexed. Thus, mass balance constraints dictate that organically
691 complexed Cu in solution will closely reflect the isotopic composition of the Cu that
692 is mobilized during weathering, while the free Cu species will be fractionated by as
693 much as -1.1‰. Consequently, in a scenario in which Zn and Cu are organically
694 complexed in pore waters, secondary mineral phases may simply scavenge the
695 isotopically light uncomplexed (or weakly-complexed) pool of Zn and Cu (as
696 proposed by Vance et al., 2016).

697

698 5.2.3 Isotope fractionation during coprecipitation with aluminous Fe oxide

699

700 An alternative mechanism to explain the light isotopic composition of the laterite
701 residue is light Zn and Cu isotope fractionation associated with precipitating Fe oxide
702 phases. For example, Viers et al. (2007) observed isotopically light Zn in laterite
703 samples from Cameroon, which they attributed to ‘ferrugination’, a term which
704 implies preferential incorporation or sorption of light isotopes in or on precipitating
705 Fe oxide phases. Suhr et al. (2018) suggested a similar process to explain isotopically
706 light Zn in the residue of a basaltic laterite from Bidar, India. We observe negative
707 correlations of $\delta^{66}\text{Zn}$ and $\delta^{65}\text{Cu}$ with Fe_2O_3 (Fig. 8), indicating that Fe oxide
708 formation may well play a role in the very light isotopic compositions of Cu and Zn in
709 zone II and IV samples.

710

711 Can ferrugination alone lead to isotopically light Zn and Cu in the laterite residue?
712 Most experimental studies have focussed upon inorganic *sorption* of Zn and Cu on Fe
713 oxide (or other mineral) surfaces, with the prevailing paradigm that such sorption is
714 typically associated with preferential accumulation of heavy isotopes on the mineral
715 surface (Pokrovsky et al., 2005; Balistrieri et al., 2008; Juillot et al., 2008; Pokrovsky
716 et al., 2008; Bryan et al., 2015; Guinoiseau et al., 2016). Preferential sorption of
717 heavy isotopes on precipitating oxide surfaces would be contrary to the observed light
718 isotopic compositions of laterite samples in zones II and IV.

719

720 The dominant Fe oxide phases present in the SQ samples are aluminous goethite and
721 aluminous haematite (Table S1; Wimpenny et al., 2007). Both phases can also
722 *incorporate* Zn^{2+} and Cu^{2+} into their structures, via substitution for Fe^{3+} on octahedral
723 (VI-fold coordinated) sites (e.g., Cornell and Giovanoli, 1988; Gerth, 1990; Manceau
724 et al., 2000; Cornell and Schwertmann, 2003). Incorporation of significant Zn (19.9
725 $\mu\text{g/g}$) and Cu (31 $\mu\text{g/g}$) in goethite and haematite, comparable to the concentrations
726 observed in the indurated SQ duricrust (Zn: 25 – 31 $\mu\text{g/g}$, Cu: 39 – 61 $\mu\text{g/g}$), has been
727 suggested for lateritic samples from Western Australia (Anand and Gilkes, 1987;
728 Singh and Gilkes, 1992). Preferential incorporation of isotopically light Zn and Cu
729 into precipitating aluminous Fe oxides could thus provide a mechanism to drive the
730 laterite residue isotopically light.

731

732 The trajectory of the dashed arrow in Figure 9A implies a maximum effective isotopic
733 fractionation factor on incorporation of Zn into Fe oxides of $\Delta^{66}\text{Zn}_{\text{Fe oxide-aqueous}} \approx -$
734 0.7‰ (Fig 9A). A conference abstract indicates that Zn incorporation in goethite may
735 indeed be associated with a preference for the light Zn isotope, though the magnitude
736 of associated isotope fractionation is not reported (Becker et al., 2014). In the case of
737 Cu, the equivalent maximum effective isotope fractionation factor described by the
738 trajectory of the dashed arrow in Figure 9B is about -1.3‰ . Experiments measuring
739 isotope fractionation on incorporation of trace metals in Fe (and other, e.g., Al) oxides
740 are an important avenue for future research.

741

742 To conclude, we postulate that a combination of strong complexation by organic
743 ligands in association with the retention of light isotopes in or on secondary
744 aluminous Fe oxide phases can explain the residual light Zn and Cu isotope signatures
745 of the zone II and IV laterite samples. If ferrugination alone is driving the light
746 isotopic composition of the laterite residue, Zn and Cu must be incorporated in (rather
747 than sorbed on) Fe oxide phases. Micro-analytical techniques, such as EXAFS, may
748 allow identification of the phase association and crystal chemistry of Zn and Cu in
749 laterite samples.

750

751 *5.2.4 Upper horizon: a role for organic matter?*

752

753 Surface organic-rich layers of soils are often enriched in light Zn and Cu isotopes,
754 which has been related to the uptake and recycling of plants (e.g., Bigalke et al., 2011,
755 2010a; Liu et al., 2014; Vance et al., 2016; Weiss et al., 2007). Therefore, the
756 presence of isotopically light solid organic matter in the uppermost sample of the SQ
757 weathering profile is plausible, given that the surface of the lateritic mesa into which
758 the quarry has been excavated is characterized by well-developed sub-tropical scrub
759 vegetation, predominantly acacia. The uppermost sample (SQ14) is slightly enriched
760 in Cu and Zn relative to the other two indurated laterite duricrust samples (SQ12 and
761 SQ13), and is indeed the isotopically lightest sample in the whole section ($\delta^{66}\text{Zn} = -$
762 0.02‰ and $\delta^{65}\text{Cu} = -0.89\text{‰}$; Figs. 3 and 4). Unfortunately, we lack sufficient
763 sampling resolution to evaluate in detail the role of recent biological activity and
764 modern soil formation in the uppermost meters of the weathering profile.

765

766 **5.3 Zone III: the Paleo-water Table**

767

768 Previous studies have noted considerable major and trace element and isotope
769 variability associated with the paleo-water table zone III (at 7 – 8.5 m depth, samples
770 SQ10 and SQ11; Howarth et al., 2018; Wimpenny et al., 2007; Widdowson, 2009),
771 which represents a transition from sub-oxic to fully oxidising conditions (Wimpenny
772 et al., 2007). There are two ways of interpreting this zone of alteration. To date, it has
773 been suggested to be at the top of a ‘classic’ groundwater level that was abandoned
774 during uplift (Wimpenny et al., 2007). As such, it is considered to have developed
775 through a combination of open system, allochthonous input of trace elements from
776 circulating groundwaters, and the precipitation of Fe and Mn-oxides, which act as
777 effective scavengers of other elements (Howarth et al., 2018; Wimpenny et al., 2007;
778 Widdowson, 2009).

779

780 An alternative interpretation suggests that zone III was at the base of an ancient,
781 episodic stagnant water body (i.e. seasonally present between the surface and ~8 m
782 depth). In this case, water would have accumulated at a depth with reduced water
783 permeability at the base of zone III during the rainy season, and zones III and IV
784 could be considered together as a single lateritized package that subsequently
785 underwent uplift, drying and hardening to form the present duricrust. In this scenario,
786 the Fe-rich mottles in zone II (i.e. at depths below ~8 m) would reflect a second phase
787 of waterlogging and lateritization, with seasonal stagnant water pooling close to the
788 present day line of seepage (at ~15 m depth). This idea, of two repeating packages of
789 lateritic alteration, could plausibly explain the τ_{Zn} , τ_{Cu} and Zn and Cu isotope data
790 (Figs. 4B, 5A). However, we would expect to observe Fe enrichment at the line of
791 seepage, equivalent to that observed in zone III (Fig. 4C), and no such Fe (or Mn)
792 enrichment is observed. Further sampling at higher resolution, and laterally within the
793 quarry, would help reconcile these two scenarios. For the purpose of this study, we
794 consider that the distinct geochemistry of the samples in zone III deserve separate
795 treatment to the more predictable upwardly progressing alteration characteristics of
796 the remainder of the profile.

797

798 Evidence for the allochthonous input of elements to zone III is demonstrated through
799 the behaviour of τ_{Fe} and τ_{Mn} values (Fig. 4C, Table 2). Both τ_{Fe} (18.9) and τ_{Mn} (5.5)

800 show extreme enrichment at 7.5m (SQ11), while τ_{Fe} (4.6) is also considerably
801 enriched at 8.5m (SQ10). The allochthonous input of elements to the profile can be
802 quantified by calculating integrated τ -values, weighting taus for each horizon (h) by
803 density (ρ) and thickness (z), following Vance et al. (2016):

804 Eqn. 6:
$$\tau_i^{\text{int}} = \frac{\sum_{h=0}^n (\tau_h \rho_h z_h)}{\sum_{h=0}^n (\rho_h z_h)}$$

805 where i refers to the element of interest (Zn or Cu). This approach assumes negligible
806 denudation (physical erosion) of the weathering profile during development.

807

808 Positive integrated $\tau_{\text{Fe}}^{\text{int}}$ (1.5) and, marginally, $\tau_{\text{Mn}}^{\text{int}}$ (0.02) values (Table 2), suggest that
809 the zone III enrichments in τ_{Fe} and τ_{Mn} cannot simply be explained by redistribution
810 of these elements vertically (from zone II or IV, depending on the location of the
811 water body) in the weathering profile. If we assume allochthonous input of Fe and Mn
812 at the paleo-water table depths and exclude these zone III samples from the integrated
813 τ calculations (giving $\tau_i^{\text{int-III}}$ values), we find a negative integrated $\tau_{\text{Mn}}^{\text{int-III}}$ (-0.21) value,
814 consistent with that calculated for $\tau_{\text{Li}}^{\text{int-III}}$ (-0.21) and $\tau_{\text{Zn}}^{\text{int-III}}$ (-0.22). $\tau_{\text{Fe}}^{\text{int-III}}$ remains
815 positive, however, at 0.36, suggesting 30 to 40% Fe addition to the weathering profile
816 during alteration.

817

818 Both Cu (52 $\mu\text{g/g}$) and Zn (97 $\mu\text{g/g}$) show enrichment in zone III, with $\tau_{\text{Cu}} = 0.8$ and
819 $\tau_{\text{Zn}} = 0.5$ at 7.5m (SQ11, Fig. 4B). Integrated $\tau_{\text{Zn}}^{\text{int}}$ and $\tau_{\text{Cu}}^{\text{int}}$ values are negative,
820 however, both including ($\tau_{\text{Zn}}^{\text{int}} = -0.23$, $\tau_{\text{Cu}}^{\text{int}} = -0.07$) and excluding ($\tau_{\text{Zn}}^{\text{int-III}} = -0.22$,
821 $\tau_{\text{Cu}}^{\text{int-III}} = -0.06$) the zone III samples (Table 2). Therefore, the enrichments of Zn and
822 Cu in zone III do not *require* an allochthonous source of these two elements, though
823 such a source is not excluded.

824

825 The enrichments in Cu and Zn in zone III are restricted to a narrow depth range,
826 sampled at SQ11 only (7.5m, Fig. 4B). This pattern is similar to the narrow band of
827 enrichment observed for Mn (Fig. 4C) and contrasts with that of Fe, which is
828 significantly elevated across both SQ10 and SQ11 (8.5 – 7.5m; Fig. 4C). Manganese
829 oxide develops large areas of negative charge under the pH conditions of natural
830 waters, as a consequence of its low pH point of zero charge and relatively high
831 specific surface area (Catts and Langmuir, 1986). These characteristics make it a very

832 effective sorbent for other trace metals (e.g., Aplin and Cronan, 1985; Balistrieri and
833 Murray, 1986; Koschinsky and Hein, 2003; Peacock and Sherman, 2007; Tessier et
834 al., 1996). Accordingly, we suggest that Cu and Zn are scavenged by a precipitating
835 Mn oxide phase at the paleo-water table, rather than by the abundant Fe oxide phases
836 (as suggested for the zone II and IV samples; section 5.2). Sequential leaching
837 experiments would be required to further test this hypothesis.

838

839 Sample SQ11 is marked by an excursion towards isotopically heavier Cu compared to
840 the samples below and above, indicating scavenging of heavy Cu (Figs. 5, 7). In the
841 case of Zn, there is no resolvable shift in $\delta^{66}\text{Zn}$ (at +0.14‰) compared to the samples
842 above and below. In both cases sample SQ11 is distinct from the coherent τ - δ trends
843 observed throughout the rest of the profile, which are reasonably well described by a
844 simple Rayleigh model (as described in Section 5.2.1; Fig. 7). There are two possible
845 explanations for the enrichment and distinct isotopic composition of SQ11: first, a
846 source with an isotopically heavy Cu isotope composition, or second, a source
847 combined with *in situ* isotope fractionation on sorption to the postulated Mn-oxide
848 phase.

849

850 Aerosols are one possible external source of trace metals to weathering profiles, and
851 are typically approximately lithogenic in Zn and Cu isotope composition ($\delta^{66}\text{Zn}$
852 \sim -0.3‰ and $\delta^{65}\text{Cu}$ \sim 0‰; Dong et al., 2013; Little et al., 2014b). Based on the data in
853 this study, a locally derived lateritic aerosol source would be very isotopically light,
854 however, inconsistent with the shift toward heavier Cu isotope compositions at the
855 depth of the paleo-water table. Further, assuming an atmospheric route for aerosol
856 deposition, any aerosol addition should also be apparent as enrichment at the surface-
857 most depths of the laterite profile; such behaviour is not observed for the SQ profile.

858

859 Solute-laden groundwater has previously been suggested as providing an external
860 source of Re, Os, and Tl, to the SQ laterite, possible due to its low-lying topographic
861 position (Howarth et al., 2018; Wimpenny et al., 2007). Relatively few constraints
862 exist on the isotopic composition of Zn and Cu in groundwater, however. An
863 isotopically heavy groundwater source of Cu is certainly plausible, given observations
864 of isotopically heavy Cu in the dissolved phase in rivers (+0.02 to +1.45‰, discharge-
865 weighted average of +0.68‰; Vance et al., 2008). A groundwater-borne source of Zn

866 at about +0.2‰ is also possible, given the range of dissolved $\delta^{66}\text{Zn}$ in global rivers (–
867 0.12 to +0.88‰, discharge-weighted average of +0.33‰; Little et al., 2014b) and
868 mountain streams (+0.02 to +0.46‰, Borrok et al., 2008). Future isotope studies
869 should target groundwater in conjunction with surface-flowing water bodies.

870

871 Isotope fractionation may occur on sorption to the postulated Mn oxide phase. Bryan
872 et al. (2015) investigated Zn isotope fractionation on inorganic sorption to synthetic
873 birnessite ($\delta\text{-MnO}_2$), a phyllosilicate phase common in terrestrial environments
874 (e.g., Taylor et al., 1964; Ross et al., 1976; Tokashiki et al., 1986; Uzochukwu and
875 Dixon, 1986; Post, 1999). At low ionic strength (applicable to freshwater
876 environments) they observe negligible Zn isotope fractionation, which is attributed to
877 the formation of octahedral surface complexes (Manceau et al., 2002); i.e. there is no
878 marked change in coordination environment on sorption compared to the hydrated
879 $\text{Zn}(\text{H}_2\text{O})_6^{2+}$ ion present in solution (Bryan et al., 2015). Sorption of ~V-fold
880 coordinated hydrated Cu^{2+} on $\delta\text{-MnO}_2$ is predicted to be associated with an
881 enrichment in heavy isotopes, due to the formation of tetrahedral surface complexes
882 (Manceau et al., 2002; Sherman and Peacock, 2010; Little et al., 2014a), though an
883 experimental study observed the opposite: preferential sorption of light Cu isotopes
884 on $\delta\text{-MnO}_2$ ($\Delta^{65}\text{Cu}_{\text{MnO}_2\text{-aqueous}} = -0.45 \pm 0.18\text{‰}$, $n=12$; Ijichi et al., 2018).

885

886 As described, the paleo-water table sample SQ11 is unusual in that it is unfractionated
887 in $\delta^{66}\text{Zn}$ and isotopically heavy in $\delta^{65}\text{Cu}$ compared to the samples above and below,
888 thus partly consistent with these inorganic predictions for sorption of hydrated Zn^{2+}
889 and Cu^{2+} on $\delta\text{-MnO}_2$. However, the system is underconstrained: we lack information
890 about the isotopic composition of the contemporaneous fluid. Speciation in the natural
891 environment is more complex compared to these inorganic experimental and
892 theoretical considerations. In future, more realistic models and experiments should be
893 designed that incorporate mixtures of organic and inorganic ligands and analogue
894 mineral surfaces.

895

896 To summarise, the distinctive Fe and Mn enrichment of the paleo-water table samples
897 supports the suggestion of open system behaviour in this zone (Wimpenny et al.,
898 2007). The observed Zn and Cu enrichment could be explained by mobilisation from
899 zones II or IV of the weathering profile or an additional groundwater-borne source,

900 with scavenging on precipitating oxide phases. Specifically, we suggest that Cu and
901 Zn are primarily scavenged by a Mn oxide phase at 7.5m depth, consistent with
902 previously published Tl isotope evidence (Howarth et al., 2018).

903

904

905 **5.4 Synthesis: Cu and Zn isotopes in the weathering environment**

906

907 *5.4.1 Integrated weathering profiles and isotope fractionation during weathering*

908

909 To draw broader conclusions regarding the behaviour of Cu and Zn during
910 lateritization, and weathering in general, we compare integrated τ -values and isotopic
911 compositions from weathering and soil profiles from diverse localities. To facilitate
912 this comparison, we normalise weathered delta values to the presumed parent material
913 (where, e.g., $\Delta^{66}\text{Zn} = \delta^{66}\text{Zn}_{\text{parent}} - \delta^{66}\text{Zn}_{\text{sample}}$) and calculate integrated $\Delta^{66}\text{Zn}_{\text{int}}$ and
914 $\Delta^{65}\text{Cu}_{\text{int}}$ values (Table 2) for the entire weathering profile in the same fashion as used
915 to calculate integrated τ -values (Eqn. 6).

916

917 The SQ laterite profile shows an integrated loss of Zn of -23% , with an integrated
918 $\Delta^{66}\text{Zn}_{\text{int}}$ of -0.14‰ (Table 2). These SQ τ - Δ data are plotted alongside data from the
919 literature in Figure 9, updating the compilation in Moynier et al. (2017, their Fig. 11).
920 Overall, Zn-depleted (negative τ_{Zn}) weathering profiles and soils show limited isotope
921 fractionation from the parent lithology. However, at the highest degrees of chemical
922 weathering, above $\sim 70\%$ Zn depletion compared to the protolith, significant
923 preferential loss of heavy Zn isotopes in three different lateritic weathering profiles is
924 observed (from India: Suhr et al., 2018 and this study; from Cameroon: Viers et al.,
925 2007).

926

927 For Cu, a smaller integrated loss of -7% from the SQ profile is calculated, with a
928 more negative $\Delta^{65}\text{Cu}_{\text{int}}$ of -0.32‰ (Table 2). There is considerably more scatter in the
929 $\tau_{\text{Cu}} - \Delta^{65}\text{Cu}$ plot (Fig. 9B) – likely due to the multiple potential processes influencing
930 Cu isotopes and to more heterogeneous protolith Cu concentrations. However, nearly
931 all Cu-depleted profiles show negative $\Delta^{65}\text{Cu}_{\text{int}}$ values (plotting in the lower left

932 quadrant of Fig. 9B), indicating consistent loss of isotopically heavy Cu during
933 weathering.
934
935 Two plausible explanations for the release of isotopically heavy Zn and Cu during
936 lateritic weathering have been discussed: (1) incorporation of light isotopes in
937 aluminous Fe oxide phases (ferrugination) or (2) organic complexation of heavy
938 isotopes in the dissolved phase. In section 5.2.1, we suggested that organic
939 complexation might lead to mobilization of heavy isotopes if mineral dissolution
940 approaches chemical equilibrium, and that this scenario would be plausible in a
941 transport-limited weathering regime. However, Figure 9 does not provide evidence
942 for the converse prediction – of mobilization of light Cu (or Zn) isotopes in
943 kinetically controlled, weathering-limited regimes (Fig. 9). Alternatively, in section
944 5.2.2, we suggested that organic complexation retains heavy isotopes in the aqueous
945 phase *after* mobilization of Cu and Zn from their host mineral phases, with sorption of
946 the complementary light pool on secondary Fe oxide minerals (section 5.2.2).

947

948 It is notable that Cu isotope data from weathering profiles developed on different
949 lithologies fall on a similar fractionation trend (Fig. 9B, dashed arrow). Mathur et al.
950 (2012) and Lv et al. (2016) favour oxidative weathering of Cu sulphides to explain
951 residual isotopically light Cu signatures observed in weathered black shales. Given
952 the absence of Cu-hosting sulphide phases in the SQ laterite, we propose that a
953 combination of organic complexation in the aqueous phase and retention of light
954 isotopes by secondary precipitating Fe oxide phases is the most likely explanation for
955 the release of heavy Cu (and Zn) isotopes during lateritization. At greater degrees of
956 Cu loss (>80%), Vance et al. (2016) observe a return towards protolith Cu isotope
957 compositions in a sequence of increasingly waterlogged basaltic soils in Hawaii (Fig.
958 9B, dotted arrow), which they attribute to reduction of Fe oxides and return of the
959 associated isotopically light Cu to the aqueous phase.

960

961 *5.4.2 Implications for the weathering-derived flux of Zn and Cu to rivers on* 962 *geological timescales*

963

964 The sensitivity of the global cycles of Zn and Cu to a change in the riverine flux
965 depends on the magnitude and timescale of the change compared to the residence time

966 of the element in the ocean. In the modern ocean, both Zn and Cu have relatively
967 short residence times of a few thousand years (Hayes et al., 2018 and references
968 therein). Thus, there is scope to influence the global ocean budgets of Zn and Cu via a
969 change in the riverine input. There are two possible ways to influence the isotopic
970 composition of the weathering-derived input of Zn and Cu to rivers: (1) change the
971 isotopic composition of the predominant weathered lithology and (2) change the
972 intensity of weathering and any associated isotope fractionation. The former is
973 unlikely to be a major control, because clastic sediments and igneous rocks have
974 restricted Zn and Cu isotope compositions (Moynier et al., 2017) and because there is
975 no consistent relationship between riverine $\delta^{66}\text{Zn}$ or $\delta^{65}\text{Cu}$ and catchment lithology in
976 modern dissolved phase river data (Vance et al., 2008; Little et al., 2014b). In this
977 contribution, we set out to address the latter, i.e. what is the maximum leverage of
978 chemical weathering on the isotopic composition of Zn and Cu supplied to rivers?
979

980 Figure 9A illustrates that significant weathering-derived Zn isotope fractionation only
981 occurs during extreme chemical weathering (lateritization). Lateritization was
982 promoted during Greenhouse climate periods of Earth history (e.g., the mid Miocene
983 Climatic Optimum), with the mid Tertiary to mid Quaternary considered to be a
984 period of particularly intensive chemical weathering (e.g., Dalvi et al., 2004; Thorne
985 et al., 2012; Widdowson, 2009). Could such a shift in weathering style have an impact
986 on the riverine $\delta^{66}\text{Zn}$ signature? While our data indicate that the Zn isotope
987 composition of the instantaneous flux to rivers from lateritic terrains can change, we
988 suggest that even widespread lateritization is unlikely to have had a major impact on
989 global average riverine $\delta^{66}\text{Zn}$. At the very high degrees of Zn mobility observed
990 during lateritic weathering, the isotopic composition of the cumulative aqueous phase
991 will approach that of the protolith by mass balance. Thus, the average Zn isotope
992 composition of the source of Zn to rivers should be rather insensitive to climate-
993 driven change on geological timescales. Nevertheless, the scope for an instantaneous
994 change in the riverine flux should be considered on short timescales and at local and
995 regional spatial scales.

996

997 The small but growing dataset for Cu isotopes during weathering indicates release of
998 isotopically heavy Cu in all oxygenated environments (Fig. 9B), consistent with the
999 observed isotopically heavy Cu in the dissolved phase of modern rivers (Vance et al.,

1000 2008). In contrast, weathering in modern reducing environments appears to re-release
1001 isotopically light Cu associated with Fe-Mn oxides (Fig. 9B; Vance et al., 2016).
1002 Periodic flooding may also lead to reduction of Cu(II) to Cu(I), with release of
1003 isotopically light Cu(I) to the aqueous phase (Bigalke et al., 2010c; Bigalke et al.,
1004 2013; Babcsányi et al., 2014). Generally, however, Cu mobility during chemical
1005 weathering is likely to be significantly reduced under anoxic conditions (e.g., Neaman
1006 et al., 2005a, 2005b). Copper and Cu isotopes may therefore be an interesting marker
1007 for the presence or absence of oxygen during the development of paleosols.

1008

1009 Finally, release of isotopically heavy Cu during weathering is consistent with the
1010 scenario outlined by Chi Fru et al. (2016) for an observed shift from relatively low to
1011 higher $\delta^{65}\text{Cu}$ values in marine sediments across the great oxidation event (GOE). This
1012 shift was interpreted to reflect release of isotopically heavy Cu from the continents on
1013 the establishment of oxidative weathering (Chi Fru et al., 2016). These authors
1014 favoured oxidative weathering of sulphides as the primary mechanism responsible for
1015 releasing heavy Cu, while our study emphasizes that weathering in an oxygenated
1016 environment promotes retention of light Cu and release of heavy Cu, regardless of the
1017 primary host phase.

1018

1019 **6.0 Conclusions**

1020

1021 We have presented evidence of systematic and correlated Zn and Cu isotope
1022 fractionation during lateritization, observing retention of light isotopes in the
1023 associated weathering profile. Zinc and Cu in the residue are likely incorporated in
1024 secondary aluminous Fe oxide phases in the laterite, a process of ‘ferrugination’ that
1025 may itself be accompanied by isotope fractionation. Alternatively, the precipitating Fe
1026 oxide phases may passively scavenge light isotopes due to preferential organic
1027 complexation of heavy isotopes in the aqueous phase. The relative roles of organic
1028 complexation versus incorporation in Fe oxide phases, and their interaction with the
1029 multitude of other controls on metal speciation in the weathering environment (e.g.,
1030 presence of inorganic ligands, pH, redox, solid organic matter) are an important target
1031 for future experimental and theoretical work.

1032

1033 Our study, taken together with those previously published, illustrates that Zn isotope
1034 fractionation during weathering is limited, except at very extreme degrees of Zn
1035 removal. Therefore, mass balance constraints limit the impact of isotopic fractionation
1036 at high degrees of chemical weathering on the $\delta^{66}\text{Zn}$ of the riverine flux. This
1037 inference is consistent with the modern measured average $\delta^{66}\text{Zn}$ in rivers, which is
1038 unfractionated from the lithogenic $\delta^{66}\text{Zn}$ value.

1039

1040 In contrast, weathering of all lithologies studied to date appears to be associated with
1041 preferential retention of isotopically light Cu, consistent with isotopically heavy Cu in
1042 the dissolved pool of rivers. Weathering alone cannot account for the isotopically
1043 heavy riverine flux on long timescales, however, due to the relatively small pool of
1044 light Cu stored in terrestrial reservoirs like soils (Vance et al., 2016). Likely, the
1045 processes responsible for the liberation of heavy Cu during weathering (or,
1046 conversely, the retention of light Cu) continue to operate in some form downstream,
1047 with partitioning between the dissolved and particulate phase maintained in rivers and
1048 the oceans.

1049

1050

1051 **Acknowledgements**

1052 The authors would like to thank four reviewers and particularly the associate editor,
1053 Matthew Fantle, for wide-ranging comments that significantly improved the original
1054 manuscript. SHL is grateful for financial support from the Leverhulme Trust (ECF-
1055 2014-615) and NERC (NE/P018181/1). This manuscript builds on the 4th year MSci
1056 project of SM at Imperial College London. We acknowledge helpful discussions with
1057 David Wilson, Dominik Weiss, Nils Suhr, Derek Vance and Brandi Revels. We are
1058 grateful to Katharina Kreissig for laboratory support and Mark Rehkämper for
1059 supplying the Zn DS. MW gratefully acknowledges Orlando Fernandes (Dhempe
1060 College, Miramar, Goa), and Sridhar Iyer (NIO, Dona Paula, Goa) for their support
1061 during fieldwork.

1062

1063 **Figure Captions**

1064

1065 **Figure 1. Left:** The location of Goa state (red) on the Indian Dharwar Craton
1066 (adapted from Paton et al., 2007). In the northeastern corner of the state, Deccan Trap
1067 flood basalts overlie the Dharwar metasediments. **Right:** The geology of Goa state
1068 (adapted from Widdowson, 2009; Devaraju et al., 2010). The black dashed line
1069 represents the state boundary. The Mercedes Quarry (SQ) laterite profile (labelled) is
1070 located at 15°28'44"N, 73°52'35"E. It is developed on Dharwar Late Archaean
1071 biotite-bearing greywacke.

1072

1073 **Figure 2. Left:** Schematic illustrating the depth distribution of samples in the laterite
1074 profile in relation to characteristic zones of alteration (Wimpenney et al., 2007;
1075 Widdowson, 2009). Graphs from left to right: Major element concentration variations
1076 (SiO_2 , Al_2O_3 , Fe_2O_3 ; Widdowson, 2009), MnO concentration variations (Widdowson,
1077 2009), and indices of alteration (Chemical Index of Alteration, CIA; Index of
1078 Lateritization, IOL; see text for further details). Grey shading highlights zone III, the
1079 paleo-water table. Samples showing only limited alteration, from below the dotted
1080 line of seepage (zone I), are paler in colour.

1081

1082 **Figure 3.** The crystal abundances of major mineral phases in the SQ laterite
1083 weathering profile compared to the four identified zones of alteration (Fig. 2;
1084 Wimpenney et al., 2007).

1085

1086 **Figure 4. A.** Concentration profiles and **B.** τ enrichment-depletion profiles (see text
1087 for details) of Li (grey triangles), Zn (red squares) and Cu (blue diamonds) in the SQ
1088 profile. **C.** τ enrichment-depletion profiles for Fe and Mn. Open symbols: little
1089 altered samples in zone I, below line of seepage (dotted line). Filled symbols: altered
1090 samples in zones II-IV, above line of seepage. Grey shaded zone III has been
1091 influenced by the paleo-water table.

1092

1093 **Figure 5. A.** Depth profiles of $\delta^{66}\text{Zn}$ (red squares) and $\delta^{65}\text{Cu}$ (blue diamonds). Open
1094 symbols: unaltered-little altered samples in zone I, below line of seepage (dotted line).
1095 Filled symbols: very increasingly altered zone II-IV mottled and lateritic samples.

1096 Shaded grey rectangle: zone III, influenced by the paleo-water table. **B.** Positive
1097 correlation between $\delta^{66}\text{Zn}$ and $\delta^{65}\text{Cu}$ in the SQ profile. Linear regression (arrow)
1098 indicates coupled loss of heavy Cu and Zn isotopes during lateritization and a
1099 resultant shift towards residual isotopically light values. Error bars represent long-
1100 term external 2SD reproducibility.

1101

1102 **Figure 6.** Covariation of Zn and Cu with selected major (A-D) and trace elements (E-
1103 H) in samples from zone I (unaltered – little altered) of the SQ laterite profile.

1104 Positive correlations of Zn with elements commonly hosted in biotite (Mg, K, Li, Co
1105 and Rb) suggest that Zn is primarily hosted in biotite in the parent greywacke (see
1106 also Fig. S3). Copper shows negative correlations with most other major and trace
1107 elements, with the exception of SiO_2 and Na_2O (Panel D), suggesting an association
1108 with a detrital phase.

1109

1110 **Figure 7.** Rayleigh fractionation modelling of **A.** Zn and **B.** Cu isotopes assuming
1111 preferential mobilization of heavy isotopes to the dissolved phase, assuming $R = R_0 \cdot f$
1112 α^{-1} (where R_0 is the isotope ratio of the protolith (larger open symbols), f the fraction
1113 removed and α the fractionation factor. For Zn: $\alpha = 1.0002$, for Cu: $\alpha = 1.001$).

1114 Dashed line: residual isotopic composition of the solid. Dash-dotted line: cumulative
1115 isotopic composition of the fluid removed from the system. Dotted line: instantaneous
1116 fluid isotopic composition. Symbols as in Figures 4 and 6. Error bars represent long-
1117 term external 2SD reproducibility. Paleo-water table sample SQ11 labelled.

1118

1119 **Figure 8.** Negative correlations of $\delta^{66}\text{Zn}$ (red squares) and $\delta^{65}\text{Cu}$ (blue diamonds)
1120 with Fe_2O_3 in the SQ profile. Paleo-water table sample SQ11 circled, other symbols
1121 as in Figure 4. Regressions are shown excluding (solid lines) and including (dashed
1122 lines) SQ11. Error bars represent long-term external 2SD reproducibility.

1123

1124 **Figure 9.** Integrated τ and integrated isotopic compositions for global weathering
1125 profiles **A.** Zn and **B.** Cu. Note, data are only included for studies where τ values are
1126 reported or can be calculated (Viers et al., 2007; Mathur et al., 2012; Liu et al., 2014;
1127 Lv et al., 2016; Vance et al., 2016). In order to include as much data as possible, but
1128 where an integrated τ -value cannot be calculated because horizon depths are not
1129 reported, either the full profile (for the central China black shale; Lv et al., 2016) or

1130 the mean and 1SD for each published profile (for the Cameroon laterite profiles; Viers
1131 et al., 2007) is shown. The SQ laterite dataset is shown as a full profile and as an
1132 integrated signature (larger symbol). Recently published full profile Zn isotope data is
1133 also included for the Bidar laterite, developed on Deccan basalt, for comparison (Zn
1134 only: Suhr et al., 2018). Literature data: [1] Viers et al. (2007), [2] Suhr et al. (2018),
1135 [3] Vance et al. (2016), [4] Lv et al. (2016), [5] Liu et al. (2014), [6] Mathur et al.
1136 (2012).
1137
1138

1139 **References**

- 1140 Aleva G. J. (1984) Lateritization, bauxitization and cyclic landscape development in
1141 the Guiana Shield. *Bauxite*, 297–318.
- 1142 Amrhein C. and Suarez D. L. (1988) The use of a surface complexation model to
1143 describe the kinetics of ligand-promoted dissolution of anorthite. *Geochim.*
1144 *Cosmochim. Acta*.
- 1145 Anand R. R. and Gilkes R. J. (1987) Iron oxides in lateritic soils from Western
1146 Australia. *Eur. J. Soil Sci.* **38**, 607–622.
- 1147 Aplin A. C. and Cronan D. S. (1985) Ferromanganese oxide deposits from the Central
1148 Pacific Ocean, I. Encrustations from the Line Islands Archipelago. *Geochim.*
1149 *Cosmochim. Acta* **49**, 427–436.
- 1150 Archer C. and Vance D. (2004) Mass discrimination correction in multiple-collector
1151 plasma source mass spectrometry: an example using Cu and Zn isotopes. *J. Anal.*
1152 *At. Spectrom.* **19**, 656. Available at: <http://xlink.rsc.org/?DOI=b315853e>.
- 1153 Archer C. and Vance D. (2008) The isotopic signature of the global riverine
1154 molybdenum flux and anoxia in the ancient oceans. *Nat. Geosci.* **1**, 597–600.
- 1155 Argast S. and Donnelly T. W. (1986) Compositions and sources of metasediments in
1156 the upper Dharwar Supergroup, South India. *J. Geol.* **94**, 215–231.
- 1157 Arnold T., Schönbacher M., Rehkämper M., Dong S., Zhao F. J., Kirk G. J. D., Coles
1158 B. J. and Weiss D. J. (2010) Measurement of zinc stable isotope ratios in
1159 biogeochemical matrices by double-spike MC-ICPMS and determination of the
1160 isotope ratio pool available for plants from soil. *Anal. Bioanal. Chem.* **398**,
1161 3115–3125.
- 1162 Babcsányi I., Imfeld G., Granet M. and Chabaux F. (2014) Copper stable isotopes to
1163 trace copper behavior in wetland systems. *Environ. Sci. Technol.* **48**, 5520–5529.
- 1164 Babechuk M. G., Widdowson M. and Kamber B. S. (2014) Quantifying chemical
1165 weathering intensity and trace element release from two contrasting basalt
1166 profiles, Deccan Traps, India. *Chem. Geol.* **363**, 56–75. Available at:
1167 <http://dx.doi.org/10.1016/j.chemgeo.2013.10.027>.
- 1168 Balistrieri L. S., Borrok D. M., Wanty R. B. and Ridley W. I. (2008) Fractionation of
1169 Cu and Zn isotopes during adsorption onto amorphous Fe(III) oxyhydroxide:
1170 Experimental mixing of acid rock drainage and ambient river water. *Geochim.*
1171 *Cosmochim. Acta* **72**, 311–328.

- 1172 Balistrieri L. S. and Murray J. W. (1986) The surface chemistry of sediments from the
1173 Panama Basin: The influence of Mn oxides on metal adsorption. *Geochim.*
1174 *Cosmochim. Acta* **50**, 2235–2243.
- 1175 Banks N. G. (1973) Biotite as a source of some of the sulfur in porphyry copper
1176 deposits. *Econ. Geol.* **68**, 697–703.
- 1177 Becker K., Catalano J. and Moynier F. (2014) Connecting Zinc Partitioning and
1178 Isotope Fractionation during Fe(II)-Catalyzed Recrystallization of Fe(III) Oxide
1179 Minerals. In *Goldschmidt Abstracts* p. 151.
- 1180 Benedetti M. F., Milne C. J., Kinniburgh D. G., Van Riemsdijk W. H. and Koopal L.
1181 K. (1995) Metal Ion Binding to Hemic Substances: Application of the Non-Ideal
1182 Competitive Adsorption Model. *Environ. Sci. Technol.* **29**, 446–457.
- 1183 Bennett P. C. (1991) Quartz dissolution in organic-rich aqueous systems. *Geochim.*
1184 *Cosmochim. Acta*.
- 1185 Bentahila Y., Othman D. Ben and Luck J.-M. (2008) Strontium, lead and zinc
1186 isotopes in marine cores as tracers of sedimentary provenance: A case study
1187 around Taiwan orogen. *Chem. Geol.* **248**, 62–82.
- 1188 Berthelin J. and Munier-Lamy C. (1983) Microbial Mobilization and Preconcentration
1189 of Uranium from Various Rock Materials by Fungi. *Ecol. Bull.*, 395–401.
1190 Available at: <http://www.jstor.org/stable/20112875>.
- 1191 Bigalke M., Kersten M., Weyer S. and Wilcke W. (2013) Isotopes trace
1192 biogeochemistry and sources of Cu and Zn in an intertidal soil. *Soil Sci. Soc. Am.*
1193 *J.* **77**, 680–691.
- 1194 Bigalke M., Weyer S., Kobza J. and Wilcke W. (2010a) Stable Cu and Zn isotope
1195 ratios as tracers of sources and transport of Cu and Zn in contaminated soil.
1196 *Geochim. Cosmochim. Acta* **74**, 6801–6813. Available at:
1197 <http://dx.doi.org/10.1016/j.gca.2010.08.044>.
- 1198 Bigalke M., Weyer S. and Wilcke W. (2010b) Copper isotope fractionation during
1199 complexation with insolubilized humic acid. *Environ. Sci. Technol.* **44**, 5496–
1200 5502.
- 1201 Bigalke M., Weyer S. and Wilcke W. (2010c) Stable copper isotopes: A novel tool to
1202 trace copper behavior in hydromorphic soils. *Soil Sci. Soc. Am. J.* **74**, 60.
- 1203 Bigalke M., Weyer S. and Wilcke W. (2011) Stable Cu isotope fractionation in soils
1204 during oxic weathering and podzolization. *Geochim. Cosmochim. Acta* **75**, 3119–
1205 3134. Available at: <http://dx.doi.org/10.1016/j.gca.2011.03.005>.

- 1206 Bonnet N. J., Beauvais A., Arnaud N., Chardon D. and Jayananda M. (2014)
1207 First⁴⁰Ar/³⁹Ar dating of intense Late Palaeogene lateritic weathering in
1208 Peninsular India. *Earth Planet. Sci. Lett.* **386**, 126–137. Available at:
1209 <http://dx.doi.org/10.1016/j.epsl.2013.11.002>.
- 1210 Borrok D. M., Nimick D. A., Wanty R. B. and Ridley W. I. (2008) Isotopic variations
1211 of dissolved copper and zinc in stream waters affected by historical mining.
1212 *Geochim. Cosmochim. Acta* **72**, 329–344.
- 1213 Brantley S. L. (2003) Reaction Kinetics of Primary Rock-forming Minerals under
1214 Ambient Conditions. In *Treatise on Geochemistry* (eds. H. D. Holland and K. K.
1215 Turekian). Elsevier. pp. 73–117.
- 1216 Brantley S. L. and Lebedeva M. (2011) Learning to Read the Chemistry of Regolith
1217 to Understand the Critical Zone. *Annu. Rev. Earth Planet. Sci.* **39**, 387–416.
1218 Available at: [http://www.annualreviews.org/doi/10.1146/annurev-earth-040809-](http://www.annualreviews.org/doi/10.1146/annurev-earth-040809-152321)
1219 [152321](http://www.annualreviews.org/doi/10.1146/annurev-earth-040809-152321).
- 1220 Brantley S. L., Liermann L. and Bullen T. D. (2001) Fractionation of Fe isotopes by
1221 soil microbes and organic acids. *Geology*.
- 1222 Brantley S. L., Liermann L. J., Guynn R. L., Anbar A., Icopini G. A. and Barling J.
1223 (2004) Fe isotopic fractionation during mineral dissolution with and without
1224 bacteria. *Geochim. Cosmochim. Acta* **68**, 3189–3204.
- 1225 Bridgestock L. J., Williams H., Rehkämper M., Larnier F., Giscard M. D., Hammond
1226 S., Coles B., Andreasen R., Wood B. J. and Theis K. J. (2014) Unlocking the
1227 zinc isotope systematics of iron meteorites. *Earth Planet. Sci. Lett.* **400**, 153–
1228 164.
- 1229 Bruland K. W. (1989) Complexation of zinc by natural organic ligands in the central
1230 North Pacific. *Limnol. Oceanogr.* **34**, 269–285.
- 1231 Bryan A. L., Dong S., Wilkes E. B. and Wasylenki L. E. (2015) Zinc isotope
1232 fractionation during adsorption onto Mn oxyhydroxide at low and high ionic
1233 strength. *Geochim. Cosmochim. Acta* **157**, 182–197. Available at:
1234 <http://dx.doi.org/10.1016/j.gca.2015.01.026>.
- 1235 Cameron V. and Vance D. (2014) Heavy nickel isotope compositions in rivers and the
1236 oceans. *Geochim. Cosmochim. Acta* **128**, 195–211. Available at:
1237 <http://dx.doi.org/10.1016/j.gca.2013.12.007>.
- 1238 Catts J. G. and Langmuir D. (1986) Adsorption of Cu, Pb and Zn by δ MnO₂:
1239 applicability of the site binding-surface complexation model. *Appl.*

1240 *Geochemistry* **1**, 255–264.

1241 Chadwick O. A., Brimhall G. H. and Hendricks D. M. (1990) From a black to a gray
1242 box—a mass balance interpretation of pedogenesis. *Geomorphology* **3**, 369–390.

1243 Chapman J. B., Weiss D. J., Shan Y. and Lemburger M. (2009) Iron isotope
1244 fractionation during leaching of granite and basalt by hydrochloric and oxalic
1245 acids. *Geochim. Cosmochim. Acta*.

1246 Chi Fru E., Rodríguez N. P., Partin C. A., Lalonde S. V., Andersson P., Weiss D. J.,
1247 El Albani A., Rodushkin I. and Konhauser K. O. (2016) Cu isotopes in marine
1248 black shales record the Great Oxidation Event. *Proc. Natl. Acad. Sci.* **113**, 4941–
1249 4946. Available at: <http://www.pnas.org/lookup/doi/10.1073/pnas.1523544113>.

1250 Coale K. H. and Bruland K. W. (1988) Copper complexation in the Northeast Pacific.
1251 *Limnol. Oceanogr.* **33**, 1084–1101.

1252 Cornell R. M. and Giovanoli R. (1988) The influence of copper on the transformation
1253 of ferrihydrite (5Fe₂O₃· 9H₂O) into crystalline products in alkaline media.
1254 *Polyhedron* **7**, 385–391.

1255 Cornell R. M. and Schwertmann U. (2003) *The iron oxides: structure, properties,*
1256 *reactions, occurrences and uses.*, John Wiley & Sons.

1257 Coutaud A., Meheut M., Viers J., Rols J. L. and Pokrovsky O. S. (2014) Zn isotope
1258 fractionation during interaction with phototrophic biofilm. *Chem. Geol.* **390**, 46–
1259 60. Available at: <http://dx.doi.org/10.1016/j.chemgeo.2014.10.004>.

1260 Coutaud M., Méheut M., Glatzel P., Pokrovski G. S., Viers J., Rols J. L. and
1261 Pokrovsky O. S. (2018) Small changes in Cu redox state and speciation generate
1262 large isotope fractionation during adsorption and incorporation of Cu by a
1263 phototrophic biofilm. *Geochim. Cosmochim. Acta* **220**, 1–18.

1264 Dalvi A. D., Bacon W. G. and Osborne R. C. (2004) The Past and the Future of
1265 Nickel Laterites. *PDAC 2004 Int. Conv.*, 1–27.

1266 Deer W. A., Howie R. A. and Zussman J. (1992) *An introduction to the rock-forming*
1267 *minerals.*, Longman Scientific & Technical Hong Kong.

1268 Dessai A. G. (2011) The geology of Goa Group: Revisited. *J. Geol. Soc. India* **78**,
1269 233–242.

1270 Devaraju T. C., Sudhakara T. L., Kaukonen R. J., Viljoen R. P., Alapieti T. T.,
1271 Ahmed S. A. and Sivakumar S. (2010) Petrology and geochemistry of
1272 greywackes from Goa-Dharwar sector, western Dharwar craton: Implications for
1273 volcanoclastic origin. *J. Geol. Soc. India* **75**, 465–487.

1274 Dideriksen K., Baker J. A. and Stipp S. L. S. (2008) Equilibrium Fe isotope
1275 fractionation between inorganic aqueous Fe(III) and the siderophore complex,
1276 Fe(III)-desferrioxamine B. *Earth Planet. Sci. Lett.* **269**, 280–290.

1277 Dong S., Weiss D. J., Strekopytov S., Kreissig K., Sun Y., Baker A. R. and Formenti
1278 P. (2013) Stable isotope ratio measurements of Cu and Zn in mineral dust (bulk
1279 and size fractions) from the Taklimakan Desert and the Sahel and in aerosols
1280 from the eastern tropical North Atlantic Ocean. *Talanta* **114**, 103–109. Available
1281 at: <http://dx.doi.org/10.1016/j.talanta.2013.03.062>.

1282 Doucet L. S., Laurent O., Mattielli N. and Debouge W. (2018) Zn isotope
1283 heterogeneity in the continental lithosphere: New evidence from Archean
1284 granitoids of the northern Kaapvaal craton, South Africa. *Chem. Geol.* **476**, 260–
1285 271. Available at: <http://dx.doi.org/10.1016/j.chemgeo.2017.11.022>.

1286 Ehrlich S., Butler I., Halicz L., Rickard D., Oldroyd A. and Matthews A. (2004)
1287 Experimental study of the copper isotope fractionation between aqueous Cu(II)
1288 and covellite, CuS. *Chem. Geol.* **209**, 259–269.

1289 Fernandez A. and Borrok D. M. (2009) Fractionation of Cu, Fe, and Zn isotopes
1290 during the oxidative weathering of sulfide-rich rocks. *Chem. Geol.* **264**, 1–12.
1291 Available at: <http://dx.doi.org/10.1016/j.chemgeo.2009.01.024>.

1292 Frei R., Poiré D. and Frei K. M. (2014) Weathering on land and transport of
1293 chromium to the ocean in a subtropical region (Misiones, NW Argentina): A
1294 chromium stable isotope perspective. *Chem. Geol.* **381**, 110–124. Available at:
1295 <http://dx.doi.org/10.1016/j.chemgeo.2014.05.015>.

1296 Fujii T. and Albarede F. (2012) Ab initio calculation of the Zn isotope effect in
1297 phosphates, citrates, and malates and applications to plants and soil. *PLoS One* **7**,
1298 0–4.

1299 Fujii T., Moynier F., Abe M., Nemoto K. and Albarède F. (2013) Copper isotope
1300 fractionation between aqueous compounds relevant to low temperature
1301 geochemistry and biology. *Geochim. Cosmochim. Acta* **110**, 29–44.

1302 Fujii T., Moynier F., Blichert-Toft J. and Albarède F. (2014) Density functional
1303 theory estimation of isotope fractionation of Fe, Ni, Cu, and Zn among species
1304 relevant to geochemical and biological environments. *Geochim. Cosmochim.*
1305 *Acta* **140**, 553–576.

1306 Gerth J. (1990) Unit-cell dimensions of pure and trace metal-associated goethites.
1307 *Geochim. Cosmochim. Acta* **54**, 363–371.

- 1308 Goldich S. S. (1938) A Study in Rock-Weathering. *J. Geol.*
- 1309 Gomez-Gonzalez M. A., Garcia-Guinea J., Laborda F. and Garrido F. (2015)
- 1310 Thallium occurrence and partitioning in soils and sediments affected by mining
- 1311 activities in Madrid province (Spain). *Sci. Total Environ.* **536**, 268–278.
- 1312 Goudie A. S. (2004) Laterite. *Encycl. Geomorphol.*
- 1313 Grybos M., Davranche M., Gruau G. and Petitjean P. (2007) Is trace metal release in
- 1314 wetland soils controlled by organic matter mobility or Fe-oxyhydroxides
- 1315 reduction? *J. Colloid Interface Sci.* **314**, 490–501.
- 1316 Guinoiseau D., Gélabert A., Allard T., Louvat P., Moreira-Turcq P. and Benedetti M.
- 1317 F. (2017) Zinc and copper behaviour at the soil-river interface: New insights by
- 1318 Zn and Cu isotopes in the organic-rich Rio Negro basin. *Geochim. Cosmochim.*
- 1319 *Acta* **213**, 178–197. Available at: <http://dx.doi.org/10.1016/j.gca.2017.06.030>.
- 1320 Guinoiseau D., Gélabert A., Moureau J., Louvat P. and Benedetti M. F. (2016) Zn
- 1321 Isotope Fractionation during Sorption onto Kaolinite. *Environ. Sci. Technol.* **50**,
- 1322 1844–1852.
- 1323 Harter R. D. and Naidu R. (1995) Role of metal-organic complexation in metal
- 1324 sorption by soils. *Adv. Agron.* **55**, 219–263.
- 1325 Hayes C. T., Anderson R. F., Cheng H., Conway T. M., Edwards R. L., Fleisher M.
- 1326 Q., Ho P., Huang K. F., John S. G., Landing W. M., Little S. H., Lu Y., Morton
- 1327 P. L., Moran S. B., Robinson L. F., Shelley R. U., Shiller A. M. and Zheng X. Y.
- 1328 (2018) Replacement Times of a Spectrum of Elements in the North Atlantic
- 1329 Based on Thorium Supply. *Global Biogeochem. Cycles* **32**, 1294–1311.
- 1330 Hibbert C. (2017) Controls on seasonal elemental variation in tropical rivers in Goa,
- 1331 India. Doctoral thesis, Birkbeck, University of London. Available at:
- 1332 <http://bbktheses.da.ulcc.ac.uk/275/>.
- 1333 Hoffmann S. R., Shafer M. M. and Armstrong D. E. (2007) Strong Colloidal and
- 1334 Dissolved Organic Ligands Binding Copper and Zinc in Rivers. **41**, 6996–7002.
- 1335 Howarth S., Prytulak J., Little S. H., Hammond S. J. and Widdowson M. (2018)
- 1336 Thallium concentration and thallium isotope composition of lateritic terrains.
- 1337 *Geochim. Cosmochim. Acta* **239**, 446–462.
- 1338 Huh Y., Chan L. H., Zhang L. and Edmond J. M. (1998) Lithium and its isotopes in
- 1339 major world rivers: implications for weathering and the oceanic budget.
- 1340 *Geochim. Cosmochim. Acta* **62**, 2039–2051.
- 1341 Ijichi Y., Ohno T. and Sakata S. (2018) Copper isotopic fractionation during

1342 adsorption on manganese oxide: Effects of pH and desorption. *Geochem. J.* **52**,
1343 e1–e6.

1344 Isson T. T., Love G. D., Dupont C. L., Reinhard C. T., Zumberge A. J., Asael D.,
1345 Gueguen B., McCrow J., Gill B. C., Owens J., Rainbird R. H., Rooney A. D.,
1346 Zhao M. Y., Stueeken E. E., Konhauser K. O., John S. G., Lyons T. W. and
1347 Planavsky N. J. (2018) Tracking the rise of eukaryotes to ecological dominance
1348 with zinc isotopes. *Geobiology* **16**, 341–352.

1349 John S. G., Kunzmann M., Townsend E. J. and Rosenberg A. D. (2017) Zinc and
1350 cadmium stable isotopes in the geological record: A case study from the post-
1351 snowball Earth Nuccaleena cap dolostone. *Palaeogeogr. Palaeoclimatol.*
1352 *Palaeoecol.* **466**, 202–208. Available at:
1353 <http://dx.doi.org/10.1016/j.palaeo.2016.11.003>.

1354 Jouvin D., Louvat P., Juillot F., Maréchal C. N. and Benedetti M. F. (2009) Zinc
1355 isotopic fractionation: Why organic matters. *Environ. Sci. Technol.* **43**, 5747–
1356 5754.

1357 Juillot F., Maréchal C., Ponthieu M., Cacaly S., Morin G., Benedetti M., Hazemann J.
1358 L., Proux O. and Guyot F. (2008) Zn isotopic fractionation caused by sorption on
1359 goethite and 2-Lines ferrihydrite. *Geochim. Cosmochim. Acta* **72**, 4886–4900.

1360 Kimball B. E., Mathur R., Dohnalkova A. C., Wall A. J., Runkel R. L. and Brantley
1361 S. L. (2009) Copper isotope fractionation in acid mine drainage. *Geochim.*
1362 *Cosmochim. Acta* **73**, 1247–1263. Available at:
1363 <http://dx.doi.org/10.1016/j.gca.2008.11.035>.

1364 Koschinsky A. and Hein J. R. (2003) Uptake of elements from seawater by
1365 ferromanganese crusts: Solid-phase associations and seawater speciation. *Mar.*
1366 *Geol.* **198**, 331–351.

1367 Kump L. R., Brantley S. L. and Arthur M. A. (2000) Chemical Weathering,
1368 Atmospheric CO₂, and Climate. *Annu. Rev. Earth Planet. Sci.* **28**, 611–667.

1369 Kunzmann M., Halverson G. P., Sossi P. A., Raub T. D., Payne J. L. and Kirby J.
1370 (2013) Zn isotope evidence for immediate resumption of primary productivity
1371 after snowball Earth. *Geology* **41**, 27–30.

1372 Larner F. and Rehkämper M. (2012) Evaluation of Stable Isotope Tracing for ZnO
1373 Nanomaterials · New Constraints from High Precision Isotope Analyses and
1374 Modeling. *Environ. Sci. Technol.* **46**, 4149–4158.

1375 Larner F., Rehkämper M., Coles B. J., Kreissig K., Weiss D. J., Sampson B.,
1376 Unsworth C. and Strekopytov S. (2011) A new separation procedure for Cu prior
1377 to stable isotope analysis by MC-ICP-MS. *J. Anal. At. Spectrom.* **26**, 1627–1632.

1378 Lebedeva M. I., Fletcher R. C. and Brantley S. L. (2010) A mathematical model for
1379 steady-state regolith production at constant erosion rate. *Earth Surf. Process.*
1380 *Landforms* **35**, 508–524.

1381 Little S. H., Sherman D. M., Vance D. and Hein J. R. (2014a) Molecular controls on
1382 Cu and Zn isotopic fractionation in Fe-Mn crusts. *Earth Planet. Sci. Lett.* **396**,
1383 213–222.

1384 Little S. H., Vance D., Walker-Brown C. and Landing W. M. (2014b) The oceanic
1385 mass balance of copper and zinc isotopes, investigated by analysis of their
1386 inputs, and outputs to ferromanganese oxide sediments. *Geochim. Cosmochim.*
1387 *Acta* **125**, 673–693.

1388 Liu S. A., Teng F. Z., Li S., Wei G. J., Ma J. L. and Li D. (2014) Copper and iron
1389 isotope fractionation during weathering and pedogenesis: Insights from saprolite
1390 profiles. *Geochim. Cosmochim. Acta* **146**, 59–75. Available at:
1391 <http://dx.doi.org/10.1016/j.gca.2014.09.040>.

1392 Lupker M., France-Lanord C., Lavé J., Bouchez J., Galy V., Métivier F., Gaillardet J.,
1393 Lartiges B. and Mugnier J. L. (2011) A Rouse-based method to integrate the
1394 chemical composition of river sediments: Application to the Ganga basin. *J.*
1395 *Geophys. Res. Earth Surf.* **116**, 1–24.

1396 Lv Y., Liu S. A., Zhu J. M. and Li S. (2016) Copper and zinc isotope fractionation
1397 during deposition and weathering of highly metalliferous black shales in central
1398 China. *Chem. Geol.* **445**, 24–35. Available at:
1399 <http://dx.doi.org/10.1016/j.chemgeo.2016.01.016>.

1400 Manceau a, Schlegel M. ., Musso M., Sole V. ., Gauthier C., Petit P. . and Trolard F.
1401 (2000) Crystal chemistry of trace elements in natural and synthetic goethite.
1402 *Geochim. Cosmochim. Acta* **64**, 3643–3661.

1403 Manceau A., Lanson B. and Drits V. A. (2002) Structure of heavy metal sorbed
1404 birnessite. Part III: Results from powder and polarized extended X-ray
1405 absorption fine structure spectroscopy. *Geochim. Cosmochim. Acta* **66**, 2639–
1406 2663.

1407 Maréchal C. and Albarède F. (2002) Ion-exchange fractionation of copper and zinc
1408 isotopes. *Geochim. Cosmochim. Acta* **66**, 1499–1509.

- 1409 Maréchal C. N., Télouk P. and Albarède F. (1999) Precise analysis of copper and zinc
1410 isotopic compositions by plasma-source mass spectrometry. *Chem. Geol.* **156**,
1411 251–273.
- 1412 Marković T., Manzoor S., Humphreys-Williams E., Kirk G. J. D., Vilar R. and Weiss
1413 D. J. (2017) Experimental Determination of Zinc Isotope Fractionation in
1414 Complexes with the Phytosiderophore 2'-Deoxymugeneic Acid (DMA) and Its
1415 Structural Analogues, and Implications for Plant Uptake Mechanisms. *Environ.*
1416 *Sci. Technol.* **51**, 98–107.
- 1417 Mathur R., Jin L., Prush V., Paul J., Ebersole C., Fornadel A., Williams J. Z. and
1418 Brantley S. (2012) Cu isotopes and concentrations during weathering of black
1419 shale of the Marcellus Formation, Huntingdon County, Pennsylvania (USA).
1420 *Chem. Geol.* **304–305**, 175–184. Available at:
1421 <http://dx.doi.org/10.1016/j.chemgeo.2012.02.015>.
- 1422 Mathur R., Ruiz J., Titley S., Liermann L., Buss H. and Brantley S. (2005) Cu
1423 isotopic fractionation in the supergene environment with and without bacteria.
1424 *Geochim. Cosmochim. Acta* **69**, 5233–5246.
- 1425 McBride M. B. (1981) Forms and distribution of copper in solid and solution phases
1426 of soil. In *Copper in Soils and Plants* (eds. J. F. Loneragan, A. D. Robson, and
1427 R. D. Graham). Academic Press: Australia.
- 1428 McBride M., Sauvé S., Hendershot W., Sauve S. and Hendershot W. (1997)
1429 Solubility control of Cu, Zn, Cd and Pb in contaminated soils. *Eur. J. Soil Sci.*
1430 **48**, 337–346.
- 1431 McFarlane M. J. (1983) Laterites. In *Chemical sediments and geomorphology*
- 1432 McFarlane M. J. (1976) Morphological mapping in laterite areas. *Stud. Geogr. Brno.*
- 1433 Moeller K., Schoenberg R., Pedersen R. B., Weiss D. and Dong S. (2012) Calibration
1434 of the New Certified Reference Materials ERM-AE633 and ERM-AE647 for
1435 Copper and IRMM-3702 for Zinc Isotope Amount Ratio Determinations.
1436 *Geostand. Geoanalytical Res.* **36**, 177–199.
- 1437 Moffett J. W. and Brand L. E. (1996) Production of strong, extracellular Cu chelators
1438 by marine cyanobacteria in response to Cu stress. *Limnol. Oceanogr.* **41**, 388–
1439 395.
- 1440 Morgan J. L. L., Wasylenki L. E., Nuester J. and Anbar A. D. (2010) Fe isotope
1441 fractionation during equilibration of Fe-organic complexes. *Environ. Sci.*
1442 *Technol.* **44**, 6095–6101.

1443 Moynier F., Vance D., Fujii T. and Savage P. (2017) The Isotope Geochemistry of
1444 Zinc and Copper. *Rev. Mineral. Geochemistry* **82**, 543–600. Available at:
1445 <http://rimg.geoscienceworld.org/lookup/doi/10.2138/rmg.2017.82.13>.

1446 Neaman A., Chorover J. and Brantley S. L. (2005a) Element mobility patterns record
1447 organic ligands in soils on early Earth. *Geology* **33**, 117–120.

1448 Neaman A., Chorover J. and Brantley S. L. (2005b) Implications of the evolution of
1449 organic acid moieties for basalt weathering over geological time. *Am. J. Sci.* **305**,
1450 147–185.

1451 Nesbitt H. W. and Young G. M. (1982) Early proterozoic climates and plate motions
1452 inferred from major element chemistry of lutites. *Nature*.

1453 Neubert N., Heri A. R., Voegelin A. R., Nägler T. F., Schlunegger F. and Villa I. M.
1454 (2011) The molybdenum isotopic composition in river water: Constraints from
1455 small catchments. *Earth Planet. Sci. Lett.* **304**, 180–190. Available at:
1456 <http://dx.doi.org/10.1016/j.epsl.2011.02.001>.

1457 Newbold T. J. (1844) Notes chiefly geological, across the Peninsula from
1458 Masulipatam to Goa, comprising remarks on the origin of regur and laterite:
1459 Occurrence of manganese veins in the latter and on certain traces of aqueous
1460 denudation on the surface of southern India. *J. Asiat. Soc. Beng.* **15**, 204–213.

1461 Nielsen S. G., Rehkämper M., Baker J. and Halliday A. N. (2004) The precise and
1462 accurate determination of thallium isotope compositions and concentrations for
1463 water samples by MC-ICPMS. *Chem. Geol.* **204**, 109–124.

1464 Opfergelt S., Cornélis J. T., Houben D., Givron C., Burton K. W. and Mattielli N.
1465 (2017) The influence of weathering and soil organic matter on Zn isotopes in
1466 soils. *Chem. Geol.* **466**, 140–148. Available at:
1467 <http://dx.doi.org/10.1016/j.chemgeo.2017.06.002>.

1468 Pascoe K. H. (1950) *A manual of the geology of India and Burma, Vol. 1.*, Govt of
1469 India, New Dehli.

1470 Paton C., Hergt J. M., Phillips D., Woodhead J. D. and Shee S. R. (2007) New
1471 insights into the genesis of Indian kimberlites from the Dharwar Craton via in
1472 situ Sr isotope analysis of groundmass perovskite. *Geology* **35**, 1011–1014.

1473 Peacock C. L. and Sherman D. M. (2007) Sorption of Ni by birnessite: Equilibrium
1474 controls on Ni in seawater. *Chem. Geol.* **238**, 94–106.

1475 Pokrovsky O. S., Viers J., Emnova E. E., Kompantseva E. I. and Freydier R. (2008)
1476 Copper isotope fractionation during its interaction with soil and aquatic

1477 microorganisms and metal oxy(hydr)oxides: Possible structural control.
1478 *Geochim. Cosmochim. Acta* **72**, 1742–1757.

1479 Pokrovsky O. S., Viers J. and Freydier R. (2005) Zinc stable isotope fractionation
1480 during its adsorption on oxides and hydroxides. *J. Colloid Interface Sci.* **291**,
1481 192–200.

1482 Pons M. L., Fujii T., Rosing M., Quitté G., Télouk P. and Albarède F. (2013) A Zn
1483 isotope perspective on the rise of continents. *Geobiology* **11**, 201–214.

1484 Post J. E. (1999) Manganese oxide minerals: Crystal structures and economic and
1485 environmental significance. *Proc. Natl. Acad. Sci.*

1486 Roser B. P., Cooper R. A., Nathan S. and Tulloch A. J. (1996) Reconnaissance
1487 sandstone geochemistry, provenance, and tectonic setting of the lower Paleozoic
1488 terranes of the West Coast and Nelson, New Zealand. *New Zeal. J. Geol.*
1489 *Geophys.*

1490 Ross S. J., Franzmeier D. P. and Roth C. B. (1976) Mineralogy and chemistry of
1491 manganese oxides in some Indiana soils. *Soil Sci. Soc. Am. J.* **40**, 137–143.

1492 Ryan B. M., Kirby J. K., Degryse F., Scheiderich K. and McLaughlin M. J. (2014)
1493 Copper isotope fractionation during equilibration with natural and synthetic
1494 ligands. *Environ. Sci. Technol.* **48**, 8620–8626.

1495 Schellman W. (1983) Geochemical principles of lateritic nickel ore formation. *Proc.*
1496 *Int. Semin. Lateritisation Process.*, 119–135. Available at:
1497 <http://ci.nii.ac.jp/naid/10003418711/en/> [Accessed October 23, 2018].

1498 Schmidt P. W., Prasad V. and Ramam P. K. (1983) Magnetic ages of some Indian
1499 laterites. *Palaeogeogr. Palaeoclimatol. Palaeoecol.* **44**, 185–202. Available at:
1500 <https://www.sciencedirect.com/science/article/pii/0031018283901025> [Accessed
1501 January 24, 2018].

1502 Schnoor J. L. (1990) Kinetics of chemical weathering: a comparison of laboratory and
1503 field weathering rates. In *Aquatic Chemical Kinetics: Reaction Rates of*
1504 *Processes in Natural Waters* (ed. W. Stumm). Zurich: Swiss Fed. Inst. Technol.
1505 pp. 475–504.

1506 Shank G. C., Skrabal S. A., Whitehead R. F. and Kieber R. J. (2004) Strong copper
1507 complexation in an organic-rich estuary: the importance of allochthonous
1508 dissolved organic matter. *Mar. Chem.* **88**, 21–39.

1509 Sherman D. M. (2013) Equilibrium isotopic fractionation of copper during
1510 oxidation/reduction, aqueous complexation and ore-forming processes:

1511 Predictions from hybrid density functional theory. *Geochim. Cosmochim. Acta*
1512 **118**, 85–97. Available at: <http://dx.doi.org/10.1016/j.gca.2013.04.030>.

1513 Sherman D. M. and Peacock C. L. (2010) Surface complexation of Cu on birnessite
1514 (δ -MnO₂): Controls on Cu in the deep ocean. *Geochim. Cosmochim. Acta* **74**,
1515 6721–6730. Available at: <http://dx.doi.org/10.1016/j.gca.2010.08.042>.

1516 Siebert C., Nagler T. F. and Kramers J. D. (2001) Determination of molybdenum
1517 isotope fractionation by double-spike multicollector inductively coupled plasma
1518 mass spectrometry. *Geochemistry, Geophys. Geosystems* **2**, 1032.

1519 Singh B. and Gilkes R. J. (1992) Properties and distribution of iron oxides and their
1520 association with minor elements in the soils of south- western Australia. *Eur. J.*
1521 *Soil Sci.* **43**, 77–98.

1522 Srinivasan R., Naqvi S. M., Raj B. U., Rao D. V. S., Balaram V. and Rao T. G. (1989)
1523 Geochemistry of the Archaean greywackes from the northwestern part of the
1524 Chitradurga schist belt, Dharwar Craton, South India-evidence for granitoid
1525 upper crust in the Archaean. *Geol. Soc. India* **34**, 505–516.

1526 Stevenson E. I., Fantle M. S., Das S. B., Williams H. M. and Aciego S. M. (2017) The
1527 iron isotopic composition of subglacial streams draining the Greenland ice sheet.
1528 *Geochim. Cosmochim. Acta* **213**, 237–254. Available at:
1529 <http://dx.doi.org/10.1016/j.gca.2017.06.002>.

1530 Suhr N., Schoenberg R., Chew D., Rosca C., Widdowson M. and Kamber B. S.
1531 (2018) Elemental and isotopic behaviour of Zn in Deccan basalt weathering
1532 profiles: Chemical weathering from bedrock to laterite and links to Zn deficiency
1533 in tropical soils. *Sci. Total Environ.* **619–620**, 1451–1463. Available at:
1534 <https://doi.org/10.1016/j.scitotenv.2017.11.112>.

1535 Swoboda-Colberg N. G. and Drever J. I. (1993) Mineral dissolution rates in plot-scale
1536 field and laboratory experiments. *Chem. Geol.* **105**, 51–69.

1537 Szyrkiewicz A. and Borrok D. M. (2016) Isotope variations of dissolved Zn in the
1538 Rio Grande watershed, USA: The role of adsorption on Zn isotope composition.
1539 *Earth Planet. Sci. Lett.* **433**, 293–302.

1540 Tardy Y. (1997) *Petrology of laterites and tropical soils.*, A.A. Balkema, Rotterdam.
1541 Available at: <https://www.cabdirect.org/cabdirect/abstract/19981913040>.

1542 Tardy Y., Kobilsek B. and Paquet H. (1991) Mineralogical composition and
1543 geographical distribution of African and Brazilian periatlantic laterites. The
1544 influence of continental drift and tropical paleoclimates during the past 150

- 1545 million years and implications for India and Australia. *J. African Earth Sci. (and*
 1546 *Middle East)* **12**, 283–295.
- 1547 Taylor G. and Eggleton R. A. (2001) *Regolith Geology and Geomorphology.*, John
 1548 Wiley & Sons.
- 1549 Taylor R. M., McKenzie R. M. and Norrish K. (1964) The mineralogy and chemistry
 1550 of manganese in some Australian soils. *Aust. J. Soil Res.* **2**, 235–248.
- 1551 Telus M., Dauphas N., Moynier F., Tissot F. L. H., Teng F.-Z., Nabelek P. I.,
 1552 Craddock P. R. and Groat L. A. (2012) Iron, zinc, magnesium and uranium
 1553 isotopic fractionation during continental crust differentiation: The tale from
 1554 migmatites, granitoids, and pegmatites. *Geochim. Cosmochim. Acta* **97**, 247–
 1555 265.
- 1556 Tessier A., Fortin D., Belzile N., DeVitre R. R. and Leppard G. G. (1996) Metal
 1557 sorption to diagenetic iron and manganese oxyhydroxides and associated organic
 1558 matter: Narrowing the gap between field and laboratory measurements.
 1559 *Geochim. Cosmochim. Acta* **60**, 387–404.
- 1560 Thorne R. L., Roberts S. and Herrington R. (2012) Climate change and the formation
 1561 of nickel laterite deposits. *Geology* **40**, 331–334.
- 1562 Tokashiki Y., Dixon J. B. and Golden D. C. (1986) Manganese Oxide Analysis in
 1563 Soils by Combined X-ray Diffraction and Selective Dissolution Methods 1. *Soil*
 1564 *Sci. Soc. Am. J.*
- 1565 Uzochukwu G. A. and Dixon J. B. (1986) Manganese oxide minerals in nodules of
 1566 two soils of Texas and Alabama. *Soil Sci. Soc. Am. J.* **50**, 1358–1363.
- 1567 Vance D., Archer C., Bermin J., Perkins J., Statham P. J., Lohan M. C., Ellwood M. J.
 1568 and Mills R. A. (2008) The copper isotope geochemistry of rivers and the
 1569 oceans. *Earth Planet. Sci. Lett.* **274**, 204–213.
- 1570 Vance D., Matthews A., Keech A., Archer C., Hudson G., Pett-Ridge J. and
 1571 Chadwick O. A. (2016) The behaviour of Cu and Zn isotopes during soil
 1572 development: Controls on the dissolved load of rivers. *Chem. Geol.* **445**, 36–53.
 1573 Available at: <http://dx.doi.org/10.1016/j.chemgeo.2016.06.002>.
- 1574 Vdović N., Bišćan J. and Juračić M. (1991) Relationship between specific surface
 1575 area and some chemical and physical properties of particulates: study in the
 1576 northern Adriatic. *Mar. Chem.* **36**, 317–328.
- 1577 Viers J., Oliva P., Nonell A., Gélabert A., Sonke J. E., Freydier R., Gainville R. and
 1578 Dupré B. (2007) Evidence of Zn isotopic fractionation in a soil-plant system of a

1579 pristine tropical watershed (Nsimi, Cameroon). *Chem. Geol.* **239**, 124–137.

1580 Weiss D. J., Boye K., Caldelas C. and Fendorf S. (2014) Zinc Isotope Fractionation
1581 during Early Dissolution of Biotite Granite. *Soil Sci. Soc. Am. J.* **78**, 171.
1582 Available at: <https://www.soils.org/publications/sssaj/abstracts/78/1/171>.

1583 Weiss D. J., Rausch N., Mason T. F. D., Coles B. J., Wilkinson J. J., Ukonmaanaho
1584 L., Arnold T. and Nieminen T. M. (2007) Atmospheric deposition and isotope
1585 biogeochemistry of zinc in ombrotrophic peat. *Geochim. Cosmochim. Acta* **71**,
1586 3498–3517.

1587 Welch S. A. and Ullman W. J. (1996) Feldspar dissolution in acidic and organic
1588 solutions: Compositional and pH dependence of dissolution rate. *Geochim.*
1589 *Cosmochim. Acta*.

1590 Welch S. A. and Ullman W. J. (1993) The effect of organic acids on plagioclase
1591 dissolution rates and stoichiometry. *Geochim. Cosmochim. Acta*.

1592 Welch S. A. and Ullman W. J. (2000) The temperature dependence of bytownite
1593 feldspar dissolution in neutral aqueous solutions of inorganic and organic ligands
1594 at low temperature (5–35°C). *Chem. Geol.*

1595 Wells M. L., Kozelka P. B. and Bruland K. W. (1998) The complexation of
1596 “dissolved” Cu, Zn, Cd and Pb by soluble and colloidal organic matter in
1597 Narragansett Bay, RI. *Mar. Chem.* **62**, 203–217.

1598 West A. J., Galy A. and Bickle M. (2005) Tectonic and climatic controls on silicate
1599 weathering. *Earth Planet. Sci. Lett.* **235**, 211–228.

1600 White A. F. and Buss H. L. (2014) Natural Weathering Rates of Silicate Minerals.
1601 *Treatise on Geochemistry*, 115–155. Available at:
1602 [https://www.sciencedirect.com/science/article/pii/B9780080959757005040?via](https://www.sciencedirect.com/science/article/pii/B9780080959757005040?via%3Dihub)
1603 [%3Dihub](https://www.sciencedirect.com/science/article/pii/B9780080959757005040?via%3Dihub) [Accessed November 16, 2018].

1604 Widdowson M. (2009) *Evolution of Laterite in Goa.*, Available at:
1605 <http://oro.open.ac.uk/19793/>.

1606 Widdowson M. (2004) Ferricrete, Ferralinitisation. In *Encyclopedia of Geomorphology*
1607 (ed. A. S. Goudie). Routledge, London. pp. 365–367.

1608 Widdowson M. (2007) Laterite and Ferricrete. In *Geochemical Sediments and*
1609 *Landscapes* (eds. D. J. Nash and S. J. McLaren). Blackwell Publishing Ltd. pp.
1610 46–94.

1611 Widdowson M. (1997) Tertiary palaeosurfaces of the SW Deccan, Western India:
1612 implications for passive margin uplift. *Geol. Soc. London, Spec. Publ.* **120**, 221–

1613 248. Available at:
1614 <http://sp.lyellcollection.org/lookup/doi/10.1144/GSL.SP.1997.120.01.15>.
1615 Widdowson M. and Gunnell Y. (1999) *Lateritization, Geomorphology and*
1616 *Geodynamics of a Passive Continental Margin: The Konkan and Kanara*
1617 *Coastal Lowlands of Western Peninsular India.*,
1618 Wiederhold J. G., Kraemer S. M., Teutsch N., Borer P. M., Halliday A. N. and
1619 Kretzschmar R. (2006) Iron isotope fractionation during proton-promoted,
1620 ligand-controlled, and reductive dissolution of goethite. *Environ. Sci. Technol.*
1621 **40**, 3787–3793.
1622 Wimpenny J., Gannoun A., Burton K. W., Widdowson M., James R. H. and Gíslason
1623 S. R. (2007) Rhenium and osmium isotope and elemental behaviour
1624 accompanying laterite formation in the Deccan region of India. *Earth Planet.*
1625 *Sci. Lett.* **261**, 239–258.
1626 Xue H. Bin, Kistler D. and Sigg L. (1995) Competition of copper and zinc for strong
1627 ligands in a eutrophic lake. *Limnol. Oceanogr.* **40**, 1142–1152.
1628

Table 1. Isotope data for USGS rock standards (mean and 2SD) analysed in this study (in grey) versus recommended (Moynier et al., 2017) or published values.

	$\delta^{66}\text{Zn}_{\text{JMC-Lyon}}$ (‰)	2SD	n	$\delta^{65}\text{Cu}_{\text{SRM976}}$ (‰)	2SD	n
BHVO-2	0.39	0.07	6	0.07	0.05	6
<i>Recommended</i>	0.28			0.12		
<i>Published Range</i>	0.21 to 0.48		7	0.10 to 0.15		5
BIR-1	0.27	0.04	3	-0.02	0.05	3
<i>Recommended</i>	0.26			0.02		
<i>Published Range</i>	0.20 to 0.36		5	-0.02 to 0.08		3
Nod P1	0.86	0.06	3	0.28	0.09	3
<i>Published Range</i>	0.78 to 0.87		3	0.29 to 0.46		3
BCR-2	0.33	0.06	3	nd		
<i>Recommended*</i>	0.25			0.17		
<i>Published Range*</i>	0.20 to 0.33		12	0.07 to 0.22		6

* Combined BCR1/2

‘n’ refers to the number of complete duplicates analysed in this study, or the number of studies compiled in the given published range.

Table 2**Table 2.** Data table, including calculated CIA and IOL values (see text for details), S concentrations, calculated τ values (where $j = \text{Nb}$, and $p = \text{SQ2-6 mean}$: see Eqn. 5 and text for details), measured Zn and Cu isotope values, and calculated Δ isotope values (where $\Delta = \delta_{\text{sample}} - \delta_{\text{SQ2}}$). Fe_2O_3 and MnO concentrations from Wimpenny et al. (2007). Li, Zn and Cu concentrations from Howarth et al. (2018).

Zone	Sample	Depth m	ρ gcm^{-3}	CIA	IOL	S $\mu\text{g/g}$	Fe_2O_3 wt%	MnO wt%	Li $\mu\text{g/g}$	Zn $\mu\text{g/g}$	Cu $\mu\text{g/g}$	$\tau_{\text{Fe,Nb}}$	$\tau_{\text{Mn,Nb}}$	$\tau_{\text{Li,Nb}}$	$\tau_{\text{Zn,Nb}}$	$\tau_{\text{Cu,Nb}}$	$\delta^{66}\text{Zn}$ ‰	2 SD	$\Delta^{66}\text{Zn}$ ‰	$\delta^{65}\text{Cu}$ ‰	2 SD	$\Delta^{65}\text{Cu}$ ‰
IV	SQ14	0	1.45	97	86	350	48.5	0.04	8.8	31	61	2.7	-0.89	-0.88	-0.87	-0.52	-0.02	0.07	-0.51	-0.87	0.07	-0.89
	SQ13	2.5	1.57	97	82	418	45.0	0.04	9.5	25	50	2.9	-0.87	-0.85	-0.89	-0.56	nd	nd	na	-0.70	0.07	-0.73
	SQ12	3.5	1.64	98	80	274	36.4	0.06	7.1	25	39	1.6	-0.85	-0.91	-0.90	-0.71	0.07	0.07	-0.42	-0.69	0.07	-0.67
	SQ12dup																nd			-0.61	0.07	
III	SQ11	7.5	1.25	95	84	203	68.3	0.57	4.2	97	52	18.9	5.5	-0.78	0.51	0.54	0.14	0.07	-0.34	-0.30	0.07	-0.32
	SQ10	8.5	1.80	96	82	408	49.6	0.02	4.5	21	31	4.6	-0.91	-0.91	-0.87	-0.64	0.15	0.07	-0.33	-0.86	0.07	-0.89
II	SQ9	12	1.29	92	31	205	10.8	0.02	8.7	23	34	0.59	-0.91	-0.77	-0.82	-0.49	0.28	0.07	-0.20	-0.60	0.07	-0.63
	SQ8	13.5	1.37	92	31	227	10.3	0.02	9.7	38	38	0.37	-0.87	-0.77	-0.73	-0.48	0.02	0.07	-0.46	-0.45	0.07	-0.47
I	SQ7	14	1.25	90	27	192	7.6	0.06	13.8	38	42	0.07	-0.64	-0.66	-0.72	-0.40	0.38	0.07	-0.11	-0.03	0.07	-0.06
	SQ6	15	2.20	59	18	630	3.4	0.05	20.2	66	53	-0.26	-0.46	-0.22	-0.23	0.19	0.42	0.07	-0.06	-0.23	0.07	-0.25
	SQ5	22.5	1.99	63	27	861	7.6	0.17	45.0	146	37	0.44	0.59	0.51	0.47	-0.29	0.53	0.07	0.05	-0.28	0.07	-0.31
	SQ4	25.5	2.23	57	15	343	2.4	0.07	12.5	33	66	-0.20	0.01	-0.27	-0.43	1.24	0.43	0.07	-0.05	-0.05	0.07	-0.08
	SQ3	30	2.68	58	22	818	5.6	0.11	32.4	115	40	-0.12	-0.22	-0.10	-0.04	-0.36	0.47	0.07	-0.01	0.04	0.07	0.02
	SQ2	34	2.75	57	23	725	6.1	0.13	31.6	112	50	0.04	0.06	-0.04	0.02	-0.12	0.51	0.07	na	0.01	0.07	na
	SQ2dup																0.48	0.07		0.04	0.07	
Dyke	SQ1	-	3.11	-	-	1634	-	-	7.4	127	122			na	na	na	0.35	0.07	na	0.08	0.07	na
Integrated (all):												1.5	0.02	-0.28	-0.23	-0.07			-0.14		-0.32	
Integrated (excl. zone III):												0.36	-0.21	-0.21	-0.22	-0.06			-0.11		-0.28	

nd – not done

na – not applicable

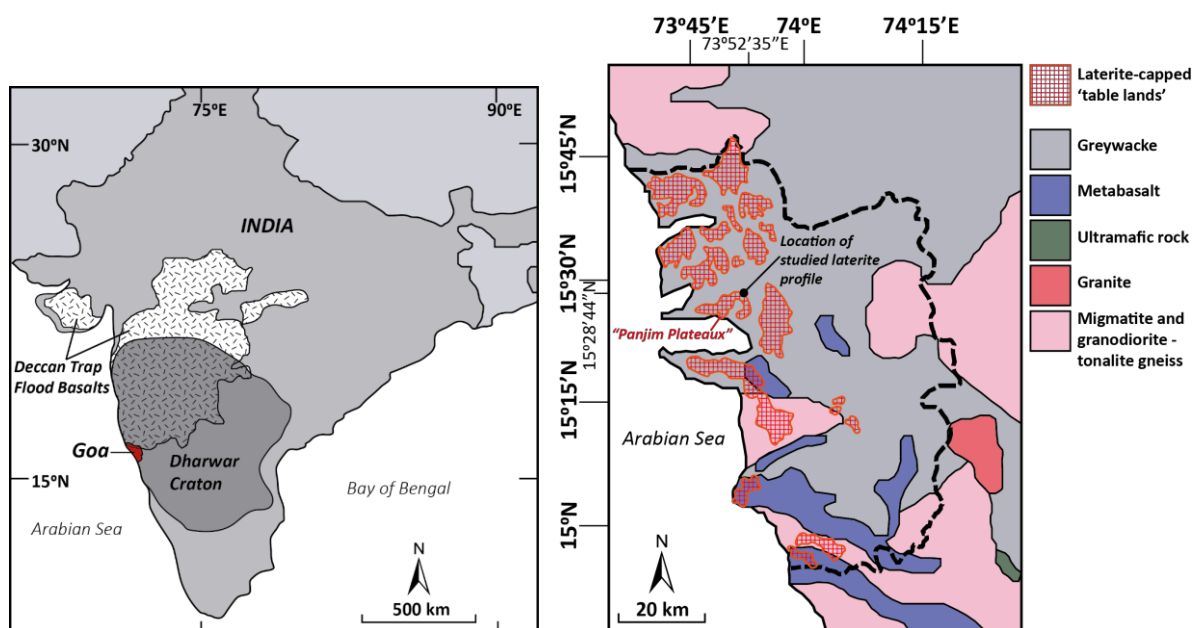


Figure 1. Left: The location of Goa state (red) on the Indian Dharwar Craton (adapted from Paton et al., 2007). In the northeastern corner of the state, Deccan Trap flood basalts overlie the Dharwar metasediments. Right: The geology of Goa state (adapted from Devaraju et al., 2010 and Widdowson, 2009). The black dashed line represents the state boundary. The Mercedes Quarry (SQ) laterite profile (labelled) is located at 15°28'44"N, 73°52'35"E. It is developed on Dharwar Late Archaean biotite-bearing greywacke.

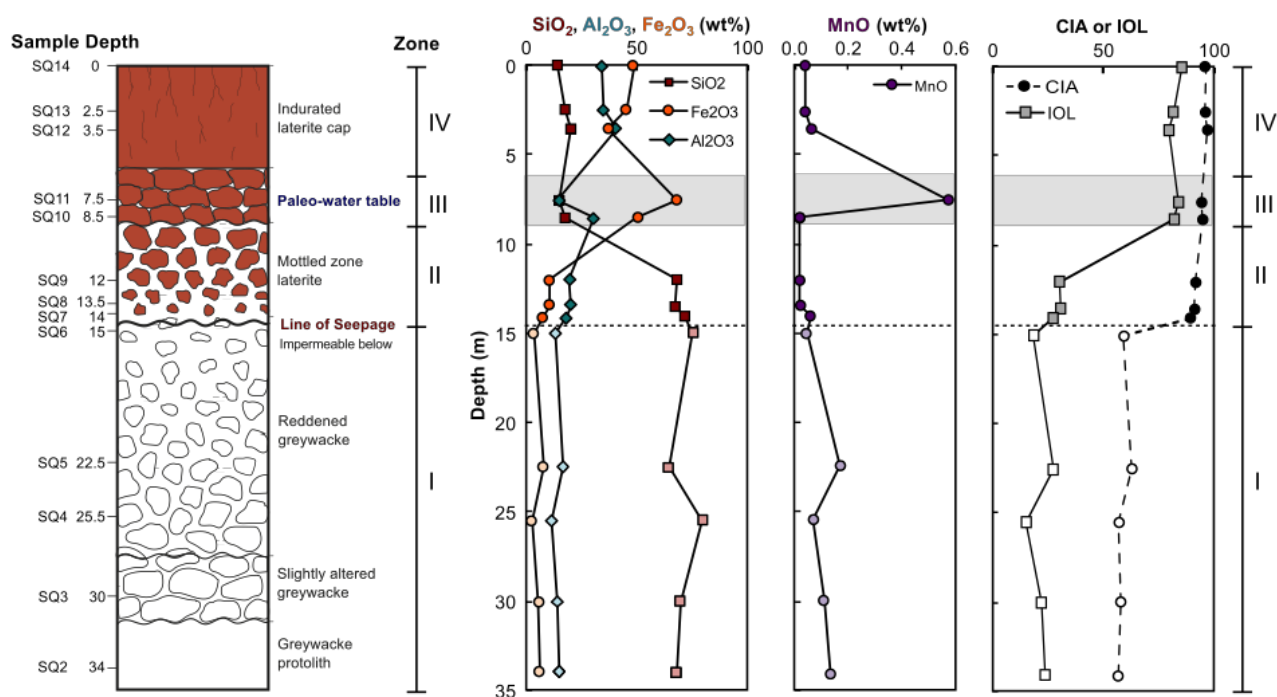


Figure 2. Left: Schematic illustrating the depth distribution of samples in the laterite profile in relation to characteristic zones of alteration (Wimpenny et al., 2007; Widdowson, 2009). Graphs from left to right: Major element concentration variations (SiO_2 , Al_2O_3 , Fe_2O_3 ; Widdowson, 2009), MnO concentration variations (Widdowson, 2009), and indices of alteration (Chemical Index of Alteration, CIA; Index of Lateritization, IOL; see text for further details). Grey shading highlights zone III, the paleo-water table. Samples showing only limited alteration, from below the dotted line of seepage (zone I), are paler in colour.

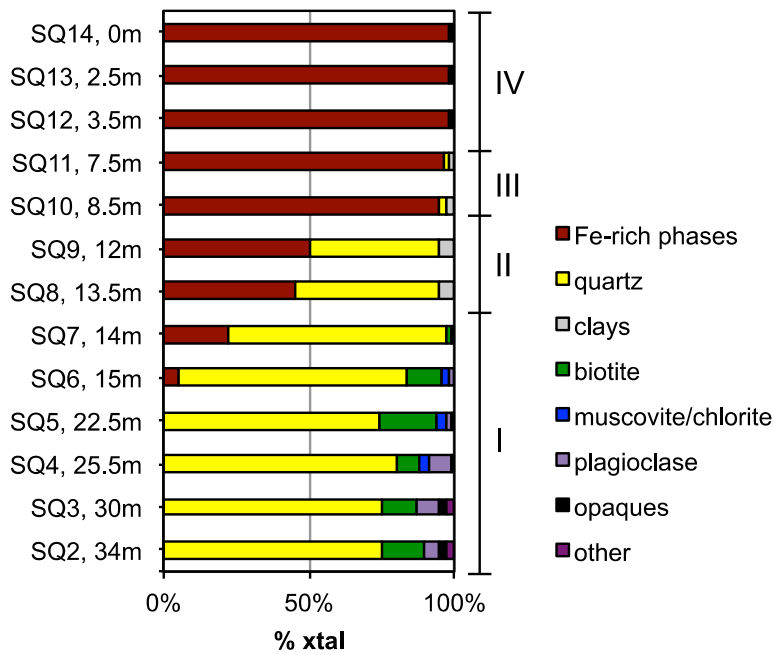


Figure 3. The crystal abundances of major mineral phases in the SQ laterite weathering profile compared to the four identified zones of alteration (see also Fig. 2; after Wimpenny et al., 2007).

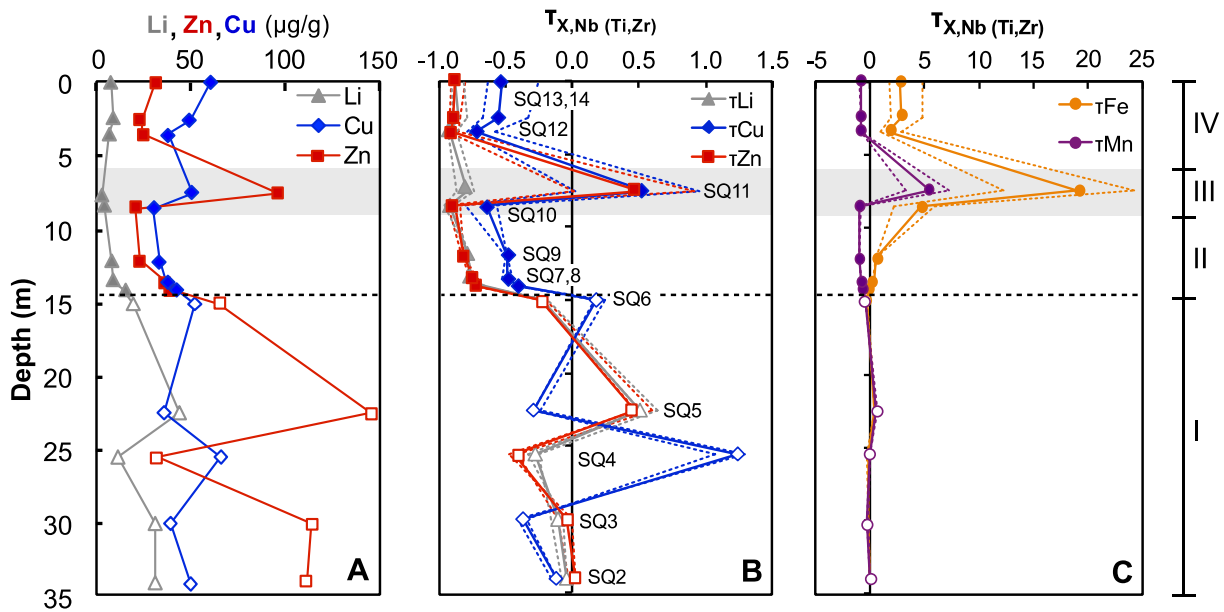


Figure 4. **A.** Concentration profiles and **B.** τ enrichment-depletion profiles (see text for details) of Li (grey triangles), Zn (red squares) and Cu (blue diamonds) in the SQ profile. **C.** τ enrichment-depletion profiles for Fe and Mn. Open symbols: little altered samples in zone I, below line of seepage (dotted line). Filled symbols: altered samples in zones II-IV, above line of seepage. Grey shaded zone III has been influenced by the paleo-water table.

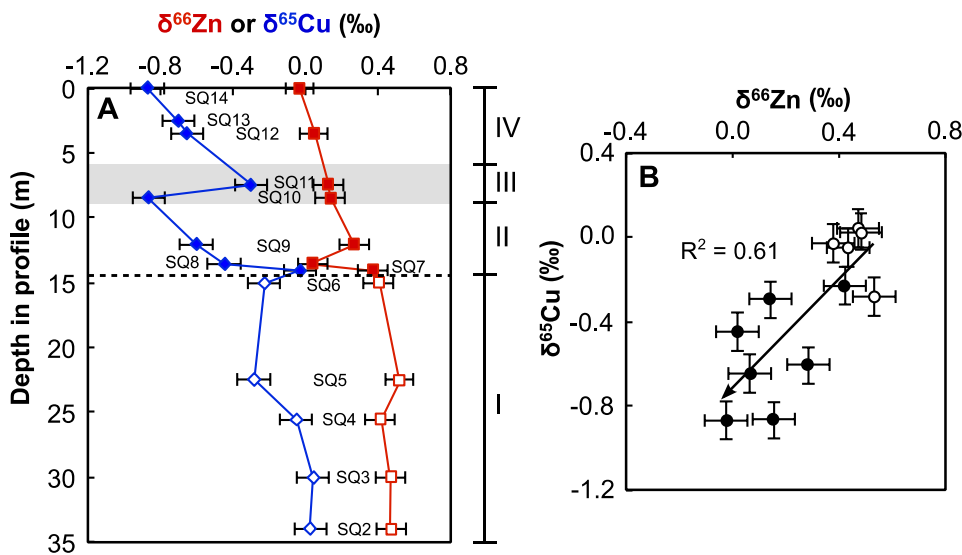


Figure 5. **A.** Depth profiles of $\delta^{66}\text{Zn}$ (red squares) and $\delta^{65}\text{Cu}$ (blue diamonds). Open symbols: unaltered-little altered samples in zone I, below line of seepage (dotted line). Filled symbols: increasingly altered zone II-IV mottled and lateritic samples. Shaded grey rectangle: zone III, influenced by the paleo-water table. **B.** Positive correlation between $\delta^{66}\text{Zn}$ and $\delta^{65}\text{Cu}$ in the SQ profile. Linear regression (arrow) indicates coupled loss of heavy Cu and Zn isotopes during lateritization and a resultant shift towards residual isotopically light values. Error bars represent long-term external 2SD reproducibility.

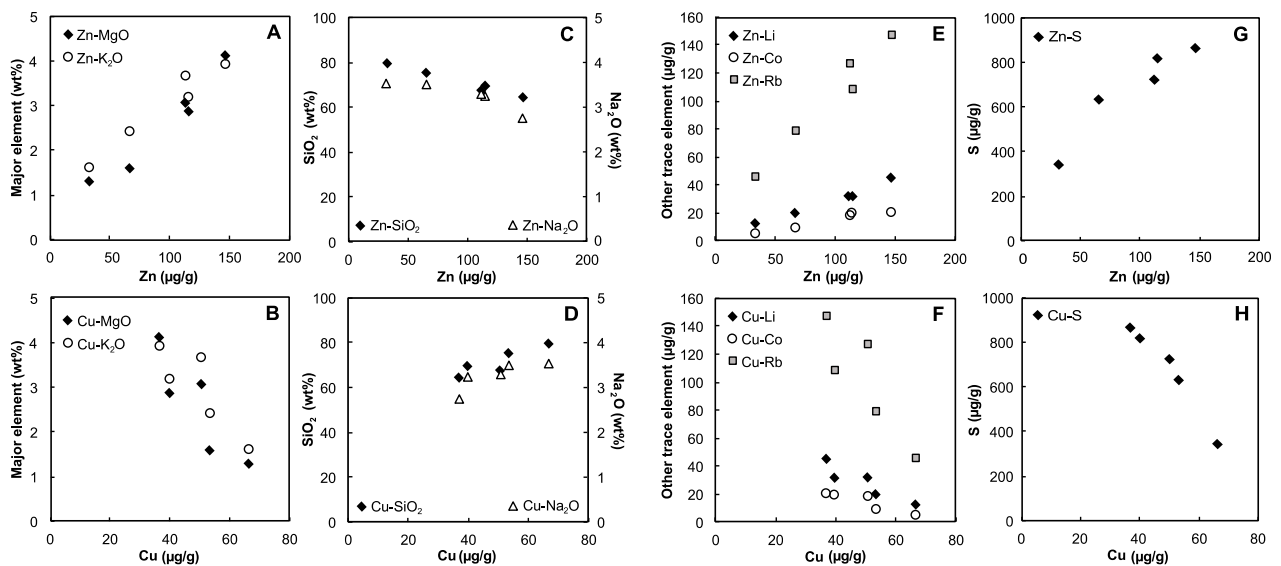
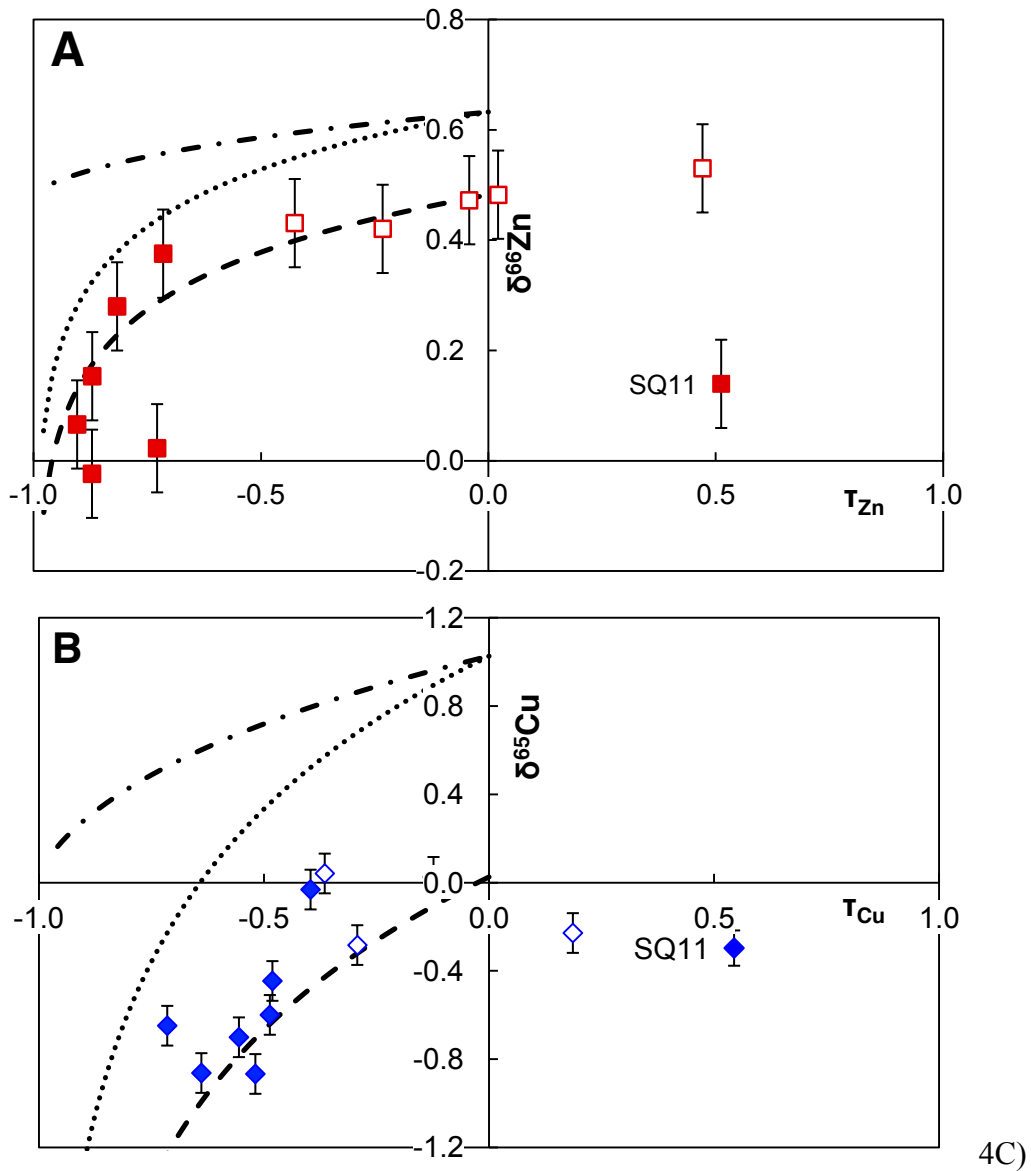


Figure 6. Covariation of Zn and Cu with selected major (A-D) and trace elements (E-H) in samples from zone I (unaltered – little altered) of the SQ laterite profile. Positive correlations of Zn with elements commonly hosted in biotite (Mg, K, Li, Co and Rb) suggest that Zn is primarily hosted in biotite in the parent greywacke (see also Fig. S3). Copper shows negative correlations with most other major and trace elements, with the exception of SiO_2 and Na_2O (Panel D), suggesting an association with a detrital phase.



4C)

Figure 7. Rayleigh fractionation modelling of **A.** Zn and **B.** Cu isotopes assuming preferential mobilization of heavy isotopes to the dissolved phase, assuming $R = R_0 \cdot f^{\alpha-1}$ (where R_0 is the isotope ratio of the protolith (larger open symbols), f the fraction removed and α the fractionation factor. For Zn: $\alpha = 1.00015$, for Cu: $\alpha = 1.001$). Dashed line: residual isotopic composition of the solid. Dash-dotted line: cumulative isotopic composition of the fluid removed from the system. Dotted line: instantaneous fluid isotopic composition. Symbols as in Figures 4 and 5. Error bars represent long-term external 2SD reproducibility. Paleo-water table sample SQ11 labelled.

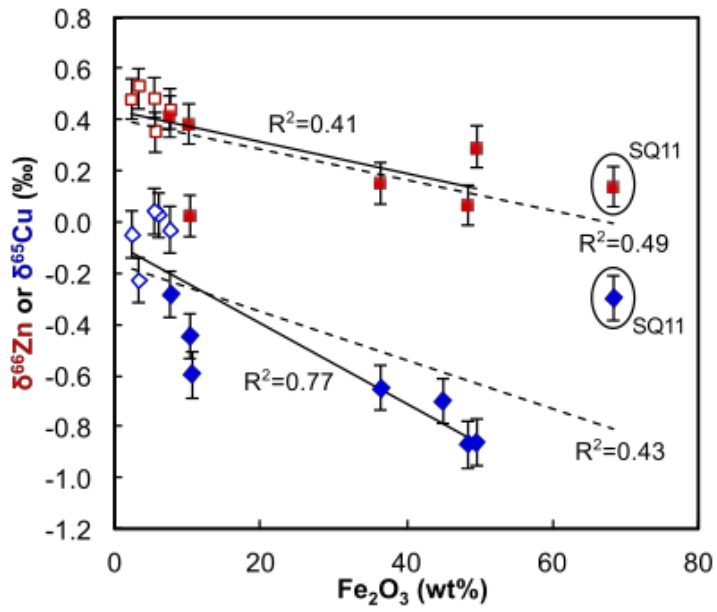


Figure 8. Negative correlations of $\delta^{66}\text{Zn}$ (red squares) and $\delta^{65}\text{Cu}$ (blue diamonds) with Fe_2O_3 in the SQ profile. Paleo-water table sample SQ11 is circled, other symbols as in Figure 5. Regressions are shown excluding (solid lines) and including (dashed lines) SQ11. Error bars represent long-term external 2SD reproducibility.

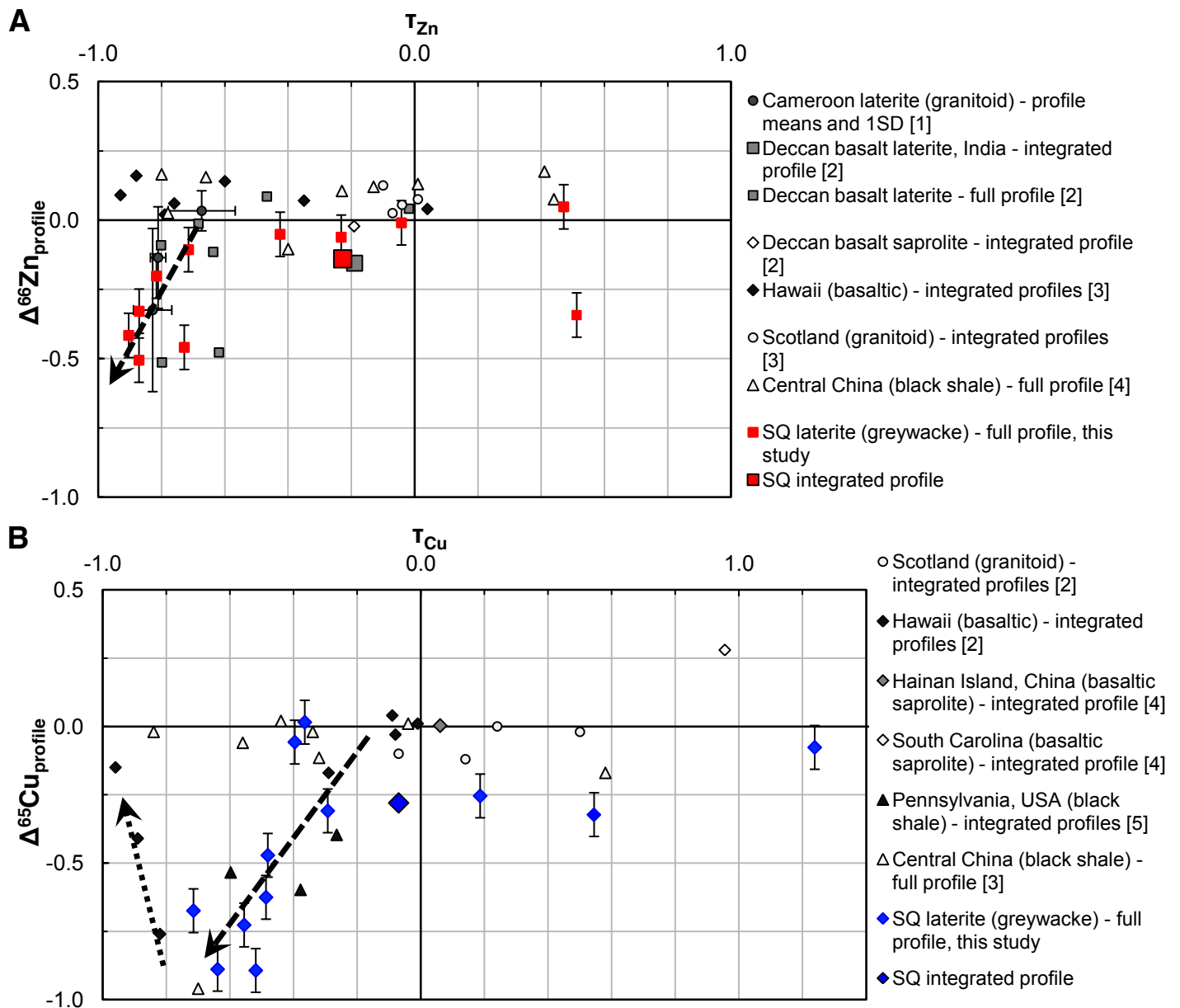


Figure 9. Integrated τ and integrated isotopic compositions for global soils **A.** Zn and **B.** Cu. Note, data are only included for studies where τ values are reported or can be calculated (Viers et al., 2007; Mathur et al., 2012; Liu et al., 2014; Lv et al., 2016; Vance et al., 2016). In order to include as much data as possible, but where an integrated τ -value cannot be calculated because horizon depths are not reported, either the full soil profile (for the central China black shale; Lv et al., 2016) or the mean and 1SD for each published profile (for the Cameroon laterite profiles; Viers et al., 2007) is shown. The SQ laterite dataset is shown as a full profile and as an integrated signature (larger symbol). Recently published full profile Zn isotope data is also included for the Bidar laterite, developed on Deccan basalt, for comparison (Zn only: Suhr et al., 2018). Literature data: [1] Viers et al. (2007), [2] Suhr et al. (2018) [3] Vance et al. (2016), [4] Lv et al. (2016), [5] Liu et al. (2014), [6] Mathur et al. (2012).

Electronic Annex

[Click here to download Electronic Annex: Revision-Electronic Supplementary Material.docx](#)